ACS Catalysis

Research Article

pubs.acs.org/acscatalysis

Flame-Made WO_3/CeO_x-TiO_2 Catalysts for Selective Catalytic Reduction of NO_x by NH_3

Katarzyna A. Michalow-Mauke,[*,†] Ye Lu,[‡,¶] Kazimierz Kowalski,[§] Thomas Graule,[∥] Maarten Nachtegaal,[†] Oliver Kröcher,[†,⊥] and Davide Ferri[*,†]

[†]Paul Scherrer Institut, CH-5232 Villigen, Switzerland

[‡]Laboratory for Solid State Chemistry and Catalysis, Empa Swiss Federal Laboratories for Materials Science and Technology, Überlandstrasse 129, CH-8600 Dübendorf, Switzerland

[§]Faculty of Metals Engineering & Industrial Computer Science, AGH University of Science & Technology, PL-30059 Krakow, Poland

[∥]Laboratory for High Performance Ceramics, Empa Swiss Federal Laboratories for Materials Science and Technology, Überlandstrasse 129, CH-8600 Dübendorf, Switzerland

[⊥]Institute of Chemical Sciences and Engineering, École polytechnique fédérale de Lausanne (EPFL), CH-1015 Lausanne, Switzerland

Supporting Information

ABSTRACT: Materials based on a combination of cerium−tungsten−titanium are potentially durable catalysts for selective catalytic NO_x reduction using NH_3 (NH_3−SCR). Flame-spray synthesis is used here to produce WO_3/CeO_x-TiO_2 nanoparticles, which are characterized with respect to their phase composition, morphology, and acidic properties and are evaluated by NH_3−SCR. HR-TEM and XRD revealed that flame-made WO_3/CeO_x-TiO_2 consists of mainly rutile TiO_2, brannerite $CeTi_2O_6$, cubic CeO_2, and a minor fraction of anatase TiO_2. These phases coexist with a large portion of amorphous mixed Ce−Ti phase. The lack of crystallinity and the presence of brannerite together with the evident high fraction of Ce^{3+} are taken as evidence that cerium is also present as a dopant in TiO_2 and is well dispersed on the surface of the nanoparticles. Clusters of amorphous WO_3 homogeneously cover all particles as observed by STEM. Such morphology and phase composition guarantee short-range Ce−O−Ti and Ce−O−W interactions and thus the high surface concentration of Ce^{3+}. The presence of the WO_3 layer and the close Ce−O−W interaction further increased the Ce^{3+} content compared to binary Ce−Ti materials, as shown by XPS and XANES. The acidity of the materials and the nature of the acid sites were determined by NH_3 temperature-programmed desorption (NH_3-TPD) and DRIFT spectroscopy, respectively. TiO_2 possesses mainly strong Lewis acidity; addition of cerium, especially the presence of surface Ce^{3+} in close contact with titanium and tungsten, induces Brønsted acid sites that are considerably increased by the amorphous WO_3 clusters. As a result of this peculiar element arrangement and phase composition, 10 wt % WO_3/10 mol % CeO_x-90 mol % TiO_2 exhibits the highest NO_x reduction efficiency, which matches that of a V_2O_5−WO_3/TiO_2 catalyst. Preliminary activity data indicate that the flame-made catalyst demonstrates much higher performance after thermal and hydrothermal aging at 700 °C than the V-based analogue despite the presence of the rutile phase. Ce^{3+} remains the dominating surface cerium species after both aging treatments, thus confirming its crucial role in NH_3−SCR by Ce−W−Ti-based catalysts.

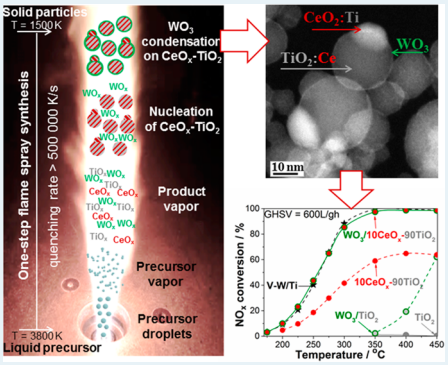

KEYWORDS: *NO_x reduction, SCR, NH_3, ceria, tungsta, titania, flame-spray synthesis, rutile*

1. INTRODUCTION

Nitrogen oxides (NO_x) are one of the major sources of air pollution, which are efficiently removed by the selective catalytic reduction using ammonia (NH_3−SCR).[1] Catalysts based on the V_2O_5−WO_3/TiO_2 system are most widely used for this purpose in mobile and stationary applications. However, this very effective catalyst system suffers from several drawbacks. Most important is its limited thermal and hydrothermal stability, which results in catalyst deactivation or even the release of vanadium species to the environment at high temperatures.[2] Therefore, there is an urgent need to develop new catalysts with better thermal and hydrothermal stability without compromising the cost-effectiveness of V_2O_5−WO_3/TiO_2 system. In the V_2O_5−WO_3/TiO_2 SCR catalyst, V_2O_5 provides redox active sites, WO_3 assures surface acidity and TiO_2 is a high surface area support, which has advantageous electronic interactions with the other components of the catalyst.[1]

Cerium oxide can also act as a redox active component in SCR catalysts due to the high redox ability of the Ce^{4+}/Ce^{3+} pair. A brief review on Ce-based SCR catalysts is given in ref 3. Bulk CeO_2 expresses some SCR activity, but its performance

Received: January 22, 2015
Revised: August 12, 2015
Published: August 14, 2015

DOI: 10.1021/acscatal.5b01580
ACS Catal. 2015, 5, 5657−5672

significantly improves when it is functionalized by transition metal ions.[4] Tungsten oxide is considered the most efficient promoter in SCR catalysts. It is reported to enhance the SCR activity and N_2 selectivity, particularly at high temperature, therefore widening the operating SCR temperature window. WO_3 also decreases ammonia and SO_2 oxidation and improves the alkali resistance.[1,5,6] A major role of WO_3 is to increase the Brønsted acidity as well as the strength and density of Brønsted acid sites,[1,6] which are involved in the SCR reaction and are important ammonia adsorption sites.[7] Moreover, WO_3 promotes the reducibility of Ce, which is beneficial to the activity of Ce-based SCR catalysts.[8] The presence and concentration of WO_3 are important, both of which significantly affect the hydrothermal stability of the SCR catalyst,[9] the type of acid sites, and catalytic activity.[10] At low tungsten oxide coverage (below 2 tungsten atoms·nm^{-2}), surface monotungstate species are predominant, and only Lewis acidity is present.[10] An increase of tungsten concentration to 3−4 tungsten atoms·nm^{-2} results in intermediate tungsten oxide coverage with formation of polytungstate species and the presence of a mixed Lewis and Brønsted acidity. Intermediate WO_x surface coverages were reported to be optimal for the NO_x reduction efficiency[11] and hydrothermal stability.[9] Further increase of the tungsten concentration (above 4 tungsten atoms·nm^{-2}) leads to formation of crystalline WO_3 nanoparticles.[10] The structure of the WO_x species on TiO_2 can be correlated to the tungsten concentration and the corresponding tungsten oxide coverage. Hilbrig et al.[12] proposed a structural model, in which islands of WO_5 are branched by WO_4 chains. At a loading below 1/3 monolayer of WO_x, mainly WO_4 units are present. With increasing tungsten concentration, the WO_5/WO_4 ratio increases, and WO_5 predominates at monolayer coverage.

In contrast to the well-established role of CeO_2 and WO_3, the function of TiO_2 in Ce−W−Ti-based catalysts appears less clear[5,8,13−15] or is confined to that of the inert but optimal metal oxide support.[5] However, the close interaction between cerium and titanium components seems to be beneficial for the SCR performance.[15−17] Currently, CeO_2−TiO_2, CeO_2−WO_3 and CeO_2−WO_3−TiO_2 catalysts have been synthesized by various techniques, for example, including wet impregnation (WI),[8,14,15] sol−gel (SG),[13,18] coprecipitation (CP),[17,19−22] or flame spray pyrolysis using an oxygen-methane flame.[23] These methods produce materials with different structural properties, ranging from fully crystalline[14,16,18,23] through partly crystalline[13,15,16,19,20] to entirely amorphous.[17] Gao et al.[16] compared CeO_2−TiO_2 obtained by WI, CP, and SG and concluded that the SG-made catalyst showed the best NH_3−SCR performance. Shan et al.[19] claimed that CP produced the best catalyst for NH_3−SCR. Generally speaking, irrespective of the synthesis method, the best performing catalysts are those in which CeO_2 is highly dispersed in the form of nanocrystallites or of an amorphous phase. In some cases, the Ce−O−Ti interaction was associated with the high CeO_2 dispersion. Li et al.[17] studied extensively the structural properties of Ce−Ti mixed oxides, revealing a predominantly amorphous nature and the existence of the brannerite $CeTi_2O_6$ phase. The good NH_3−SCR performance was interpreted as the result of the Ce−O−Ti short-range order in the amorphous materials. An increase in crystallinity, for example, by segregation of ceria and titania obtained upon treatment at 650 °C, significantly decreased the catalytic activity. CeO_2 crystallites were particularly deleterious to activity, an observation which represents a matter of debate.[14,16]

The relative arrangement of each phase and element in the material is a key factor that is not extensively addressed. In the case of wet-impregnated[15] or coimpregnated[8,14] catalysts, TiO_2 is impregnated with precursors of cerium alone or in combination with tungsten. In such materials, no strong interaction of TiO_2 with the other components is expected, whereas the interaction between well-dispersed cerium and tungsten oxide phases is considered decisive.[14,20] The situation is more complex for catalysts obtained by the SG[13,18] or the CP[17,19,20] methods because of the one-pot approach used for synthesis. Therefore, besides the NH_3−SCR performance of potentially novel SCR catalysts, it is also crucial to investigate in detail their structure, phase composition, and the relation between each catalyst component. The choice of synthesis techniques is decisive in this respect in order to be able to precisely control the phase composition and arrangement of each component to design a material with the desired catalytic properties. Flame spray synthesis (FSS) was chosen for material synthesis because it affords nanosized catalysts in a well controllable one-step process.[24−29] FSS allows obtaining unique material compositions and thus particle properties as a result of the high flame temperature and the fast quenching rate. The one-step synthesis approach ensures close interaction of the components already at the synthesis level, which may not be identical to the result obtained with conventional methods. In fact, we have shown in a preliminary work that the material properties (e.g., phase composition and morphology) of Ce−W−Ti mixed oxides obtained by an oxygen-acetylene flame cannot be reproduced by wet-impregnation to simulate the relative spatial arrangement of the various components.[30] Importantly, this results in significant catalytic characteristics for the target reaction.

The major objective of this work is to characterize the structure of various flame-made WO_3/CeO_x-TiO_2 mixed oxide catalysts with respect to morphology, relative speciation, and arrangement of the three elements cerium, tungsten, and titanium. The catalyst composition was varied with respect to the cerium loading because cerium is considered to be the active component for by NH_3−SCR. Based on the peculiar nanostructure obtained by flame synthesis, we try to identify its role in the determination of the catalytic performance for NH_3−SCR. Because of the importance of stabilizing a NH_3−SCR catalyst against high-temperature exposure, preliminary results are also reported, which demonstrate the superior performance of the most active flame-made catalyst compared to a V-based analogue.

2. EXPERIMENTAL SECTION

2.1. Catalyst Synthesis. A series of *n*mol % CeO_x − (100 − *n*)mol % TiO_2 and 10 wt % WO_3/ *n*mol % CeO_x − (100 − *n*)mol % TiO_2 nanopowders with *n* = 0, 5, 10, and 20 were prepared by flame-spray synthesis (FSS) using an oxygen-acetylene flame. Titanium diisopropoxide bis(acetylacetonate) ($TiC_{16}H_{28}O$, 75% in isopropanol, ABCR), cerium(III) ethylhexanoate ($Ce[OOCCH(C_2H_5)C_4H_9]_3$, Ce content: 11.8−12.2%, Shepherd) and tungsten carbonyl ($W(CO)_6$, Sigma-Aldrich) dissolved in tetrahydrofuran (Sigma-Aldrich) were used as Ti, Ce, and W precursors, respectively. Details of the FSS setup are reported elsewhere.[31,32] The required composition was obtained by adjusting the ratio of the different precursors in the precursor mixture, whose total flow rate was

DOI: 10.1021/acscatal.5b01580
ACS Catal. 2015, 5, 5657−5672

in the range of 0.333 $cm^3 \cdot s^{-1}$. The total precursor concentration in the flame was kept constant at 0.5 $mol \cdot kg^{-1}$. The precursor solution was fed by a syringe pump and was atomized by oxygen (583 $cm^3 \cdot s^{-1}$) in a gas-assisted external mixing nozzle. The combustible aerosol was ignited by six oxygen-acetylene flamelets (C_2H_2, 217 $cm^3 \cdot s^{-1}$; O_2, 283 $cm^3 \cdot s^{-1}$), and the produced particles were collected on glass fiber filters (GF/A 150, Whatman) using vacuum pumps. The composition and designation of the investigated materials are given in Table 1.

A 2.4 wt % V_2O_5/10 wt % WO_3/TiO_2 catalyst (V−W/Ti) was prepared by consecutive wet impregnation of TiO_2 by WO_3 and V_2O_5 precursors for the sake of comparison. This material has been shown to be a highly active NH_3−SCR catalyst.[2]

2.2. Characterization of the Catalysts. *2.2.1. Morphology and Structure.* The specific surface area (SSA) of as-prepared powders was determined by Brunauer−Emmett−Teller (BET) method from a 11-point N_2 adsorption isotherm using a Quantachrome Autosorb 1C instrument. Prior to analysis, powder samples were dried for 120 min at 180 °C in N_2.

The morphology of the catalysts was observed using a Jeol 2200FS transmission electron microscope equipped with a 200 kV field emission gun and a high-angle annular dark field (HAADF) detector in STEM mode. The local composition was determined by energy dispersive X-ray spectroscopy (EDS). The EDS spectra were normalized with the position and the intensity of the Cu K peak. The samples were prepared by deposition via an ethanol suspension onto a carbon film coated copper grid (Plano GmbH). The interplanar distance (d) was measured by averaging the distances between successive peaks in the contrast profile taken along a line perpendicular to the fringes in the software DigitalMicrograph.[33]

X-ray diffraction (XRD) analysis was performed using a Bruker D8 Advance diffractometer equipped with a Ni-filtered Cu Kβ radiation and a LinxEye detector. The diffraction patterns were collected in the range of $5° < 2\theta < 80°$. The phase identification was based on inorganic crystal structure database (ICSD) data files. Flame-made CeO_2, TiO_2 and TiO_2 aged at 700 °C (TiO_2T700) were used as reference materials for phase assignment.

2.2.2. Chemical Composition. The surface composition of the samples and the chemical states of detected elements were studied by X-ray photoelectron spectroscopy (XPS) using an instrument from VSW (Vacuum Systems Workshop) equipped with a concentric hemispherical electron analyzer with a radius of 150 mm and a two-plate 18-channel detector (Galileo). The electron analyzer was operated in the fixed-analyze transmission mode (FAT) with constant pass energy of 22 eV. Samples were exposed to Kα Al (1486.6 eV) X-ray radiation produced by an X-ray lamp working at a power of 210 W (U = 15 kV, emission current = 14 mA). The background pressure during the analyses was less than 5×10^{-8} mbar. Calibration of the binding energy scale was done by aligning the position of the Ti $2p_{3/2}$ peak in TiO_2 to 458.7 eV taken from the NIST database[34] (Figure S3a).

X-ray absorption near edge structure (XANES) spectra of pellets were recorded at the Ce L_3-edge (5.723 keV) in fluorescence mode at beamline SuperXAS of the Swiss Light Source (SLS, Villigen, Switzerland) using a 4-element Si drift diode detector. $Ce(NO_3)_3$ and CeO_2 were used as references for Ce^{3+} and Ce^{4+}, respectively, and were measured both in transmission and fluorescence mode. The self-absorption correction, the normalization, and the linear combination fit of the resulting XANES spectra were performed using the Athena software package.[35] The edge energy (E_0) was set to the maximum of the first derivative.

The chemical composition of the catalysts was investigated by inductively-coupled plasma−optical emission spectrometry (ICP-OES, Varian, type VISTA Pro AX). Prior to analysis samples were digested in a mixture of 96% H_2SO_4 and 30% H_2O_2 (Sigma-Aldrich) on the hot plate and then diluted by Milli-Q-water.

2.2.3. Surface Acidity. NH_3 temperature-programmed desorption (NH_3-TPD) was applied to assess the surface acidity of the catalysts and the NH_3 uptake (normalized by mass and SSA of the material). NH_3-TPD was performed in a quartz tube plug flow reactor prepared identically to the catalytic tests with 50 mg of catalyst diluted with 500 mg of cordierite under a total flow of 100 $mL \cdot min^{-1}$ (GHSV= 120 $L \cdot g^{-1} \cdot h^{-1}$). Prior to TPD, the sample was pretreated with 10 vol % O_2 in N_2 at 500 °C for 1 h at a ramp of 10 $°C \cdot min^{-1}$ and cooled to 50 °C in N_2. Then, NH_3 (1000 ppm in N_2) was supplied for adsorption at 50 °C for 1 h followed by N_2 flow at 50 °C for 1 h to remove weakly adsorbed species. NH_3-TPD was carried out by heating from 50 to 500 °C at 10 $°C \cdot min^{-1}$ under N_2 flow. The gas composition was monitored online by FTIR spectroscopy (Antaris, Thermo Scientific).

The nature of the active sites was determined by NH_3 adsorption using diffuse reflectance infrared Fourier transform (DRIFT) spectroscopy. All DRIFT spectra were collected at a resolution of 4 cm^{-1} using a Vertex 70 spectrometer (Bruker) equipped with a Praying Mantis mirror accessory (Harrick) and a liquid nitrogen cooled MCT detector. The sample was dried at 500 °C for 1 h in a muffle oven. Then it was transferred to the homemade DRIFT cell equipped with a CaF_2 window and further dried at 200 °C overnight in flowing N_2 (100 mL/min) prior to NH_3 adsorption. NH_3 adsorption was performed by flowing 500 ppm of NH_3 in N_2 (100 mL/min) at 50 °C for 30 min followed by flowing N_2. Consecutive spectra were recorded at 80 kHz scanner velocity at 1 min interval to follow NH_3 adsorption. All spectra are reported against a background spectrum acquired at 50 °C in N_2 prior to NH_3 adsorption.

2.3. Catalytic Test. NH_3−SCR experiments were conducted in a quartz tube plug flow reactor loaded with 10 mg of catalyst, mixed with 500 mg of 100−160 μm cordierite and firmly fixed between two quartz wool plugs. A thermocouple was inserted at the front end of the catalyst bed. The sample was pretreated with 10 vol % O_2/N_2 at 450 °C for 45 min. The model gas feed for the activity test was composed of 10 vol % O_2, 5 vol % H_2O, 1000 ppm of NO, 1200 ppm of NH_3 and balance N_2. For NH_3 and NO oxidation experiments, the feed gas consisted of 1000 ppm of NH_3 or NO, respectively, in 10 vol % O_2, 5 vol % H_2O, and balance N_2. For all experiments, the gas flow rate was 100 $mL \cdot min^{-1}$ (GHSV = 600 $L \cdot g^{-1} \cdot h^{-1}$), if not otherwise mentioned.

The gas composition was monitored online by FTIR spectroscopy (Antaris, Thermo Scientific). The NO_x conversion expressed as NO_x reduction efficiency ($deNO_x$) was calculated as follows:

$$deNO_x = \frac{NO_{x,in} - NO_{x,out}}{NO_{x,in}} \quad (1)$$

with

$$NO_x = C_{NO_2} + C_{NO} \quad (2)$$

DOI: 10.1021/acscatal.5b01580
ACS Catal. 2015, 5, 5657−5672

Table 1. Composition, Specific Surface Area (SSA), WO_3 Coverage, and Normalized NH_3 Uptake of the Flame-Made Catalysts and Reference V−W/Ti

sample name	composition	SSA/$m^2 \cdot g^{-1}$	WO_3 coverage/W atoms·nm^{-2}	WO_3 coverage[a] /%	NH_3 uptake/ppm·m^{-2}
V−W/Ti	2.4 wt % V_2O_5-10 wt % WO_3/TiO_2	60.5	4.3	95	6771
TiO_2	TiO_2	93.3	-	-	6820
10Ce-90Ti	10 mol % CeO_x-90 mol % TiO_2	95.6	-	-	4708
20Ce-80Ti	20 mol % CeO_x-80 mol % TiO_2	74.8	-	-	4520
W/TiO_2	10 wt % WO_3/ TiO_2	89.9	2.9	64	7047
W/5Ce-95Ti	10 wt % WO_3/ 5 mol % CeO_x-95 mol % TiO_2	94.4	2.8	61	6458
W/10Ce-90Ti	10 wt % WO_3/ 10 mol % CeO_x-90 mol % TiO_2	94.0	2.9	64	5540
W/20Ce-80Ti	10 wt % WO_3/ 20 mol % CeO_x-80 mol % TiO_2	77.1	3.4	75	4575

[a]One WO_3 monolayer corresponds to 4.5 tungsten atoms·nm^{-2}[10]

The selectivity for the formation of N_2O, NO_x, or N_2 during NH_3 oxidation was defined by the following equations:

$$S_{N_2O} = \frac{2 \cdot C_{N_2O,out}}{C_{NH_3,in} - C_{NH_3,out}} \times 100\% \quad (3)$$

$$S_{NO_x} = \frac{C_{NO_x,out}}{C_{NH_3,in} - C_{NH_3,out}} \times 100\% \quad (4)$$

$$S_{N_2} = 100 - (S_{NO_x} + S_{N_2O}) \quad (5)$$

The reaction rate constant k ($cm^3 \cdot g^{-1} \cdot s^{-1}$) was calculated under the assumption that the reaction is first order with respect to NO and zeroth order with respect to NH_3, which is borrowed from kinetic studies on V-based SCR catalysts:[1,21,36,37]

$$k = \frac{V}{m} \times \ln(1 - \mathrm{deNO}_x) \quad (6)$$

where V is the total gas flow ($cm^3 \cdot s^{-1}$) at temperature T (K), and m is the catalyst mass in the reactor (g). The zeroth order with respect to NH_3 was ensured by using an excess of NH_3 (1200 ppm) with respect to NO_x dosage (Figure S1).[36,37]

2.4. Thermal and Hydrothermal Aging. The sample (150 mg) was heated to 700 °C in a muffle oven within 2 h followed by dwelling for 15 h and then cooling to room temperature over 3 h. Thermal treatment (T) was carried out under ambient atmosphere, whereas hydrothermal treatment (HT) was carried out under 10 vol % H_2O in ambient atmosphere.

3. RESULTS

3.1. Composition and Structural Properties. *3.1.1. Morphology and Structure.* The SSA of all investigated powders was in the range 75−94 $m^2 \cdot g^{-1}$ and decreased with increasing Ce content in Ce−Ti and W/Ce−Ti (Table 1). This behavior is related to an increase of the overall density of the nanoparticles due to the transformation of TiO_2 from the anatase (density, 3.78 $g \cdot cm^{-3}$) to the rutile (4.23 $g \cdot cm^{-3}$) phase (vide infra). The average particle density also contributes to the decrease of SSA. Because during flame-spray synthesis (FSS) the total concentration of the precursors mixture in the flame is constant irrespective of the composition of the final product, the increase of cerium content causes an increase of product density (CeO_2 has a higher density, 7.21 $g \cdot cm^{-3}$) and the progressive decrease of the specific surface area expressed in $m^2 \cdot g^{-1}$.

Flame-made materials consist of spherically shaped nonporous particles with an average particle size of around 20 nm for unmodified TiO_2 (Figure 1a) and of around 16 nm for

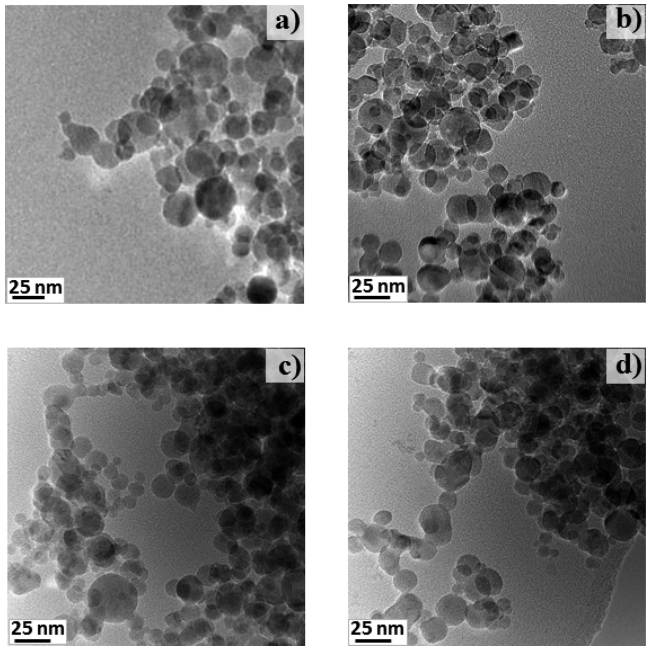

Figure 1. TEM images of (a) TiO_2, (b) W/TiO_2, (c) 10Ce-90Ti, and (d) W/10Ce-90Ti.

modified TiO_2 (Figure 1b−d). The particle size distribution of 5−35 nm is typical for flame-made materials and originates from the nature of the synthesis technique.[24,31,32]

Crystalline nanoparticles with clearly visible lattice fringes can be observed in the high resolution transmission electron microscopy (HR-TEM) images of W/10Ce-90Ti (Figure 2). Based on interplanar distance (d) analysis, four phases have been identified in the crystalline regions of the sample: anatase TiO_2, rutile TiO_2, cubic CeO_2, and brannerite ($CeTi_2O_6$).

The CeO_2 particles possess an extended interface with the rutile TiO_2 particles, suggesting the growth of CeO_2 out of the TiO_2 structure. Contrary to the typical cubic morphology of CeO_2 particles, these particles are clearly round-shaped, which suggests a great fraction of defects, likely induced by the underlying rutile TiO_2 structure. It is also important to underline that the ceria particles have always been observed only associated with rutile TiO_2. The anatase nanoparticles observed by TEM are never associated with ceria particles. The growth of cubic CeO_2 particles on the spherical rutile particles

DOI: 10.1021/acscatal.5b01580
ACS Catal. 2015, 5, 5657−5672

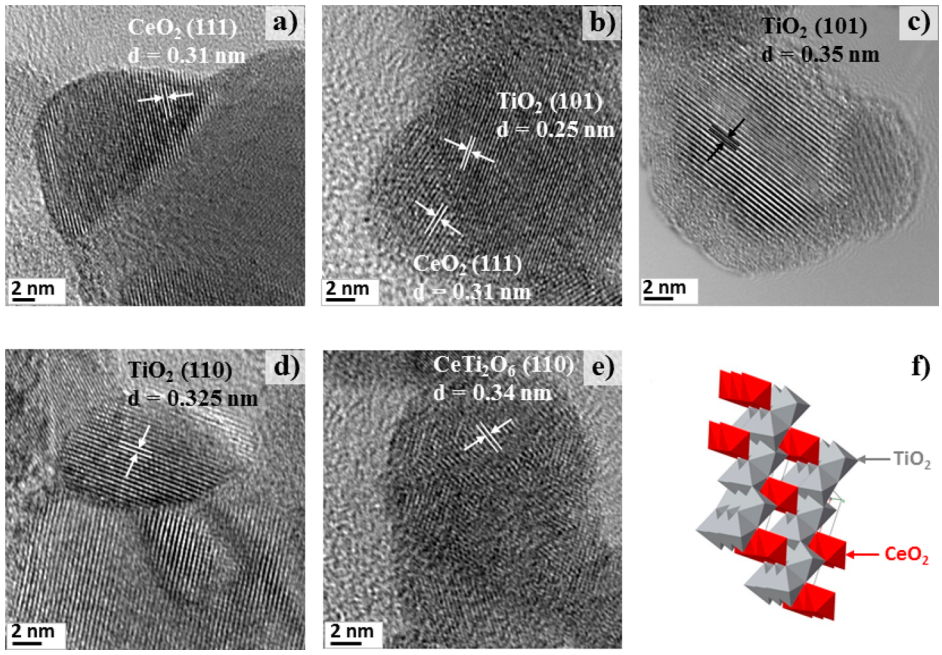

Figure 2. HR-TEM images of W/10Ce-90Ti. The various images show lattice fringes of (a) cubic CeO_2, (b) cubic CeO_2 and rutile TiO_2, (c) anatase TiO_2, (d) rutile TiO_2, (e) $CeTi_2O_6$ (brannerite). (f) Visualization of the crystal structure of $CeTi_2O_6$.

was most likely caused by strain resulting from their lattice mismatch (cubic vs tetragonal). Due to its large ionic radius cerium is forced out of the lattice sites onto the rutile surface, which can accommodate isolated cerium atoms as theoretically predicted.[38] The CeO_2 particles probably grew layer by layer. Johnston-Peck et al.[39] investigated theoretically and experimentally fluorite cubic CeO_2 grown on anatase and observed that due to the strain generated by the lattice mismatch, elongated islands of CeO_2 similar to those observed in Figure 2a grow epitaxially (i.e., layer by layer) on TiO_2, which form facilitates elastic relaxation of the stress. In addition to epitaxial growth, interdiffusion of titanium into cerium at the CeO_2–TiO_2 interface was reported that is followed by formation of stable oxygen vacancies and Ce^{3+},[39] which correlates well with the defect structure of flame-made catalysts as discussed later in this section. Fang et al.[40] demonstrated that CeO_2 initially nucleates at the oxygen vacancies of anatase by forming an interface consisting of oxygen bridges between CeO_2 and anatase, thus inhibiting the anatase-to-rutile transformation. At higher CeO_2 content, the growth of CeO_2 clusters and the formation of cubic CeO_2 nanocrystals were observed. Although attention must be given to the fact that cerium is generally deposited on anatase rather than rutile in these works, a similar mechanism can be used to interpret our observation, with the key difference that rutile is the support of the ceria particles in these flame-made materials.

The ceria–rutile interaction could explain the formation of brannerite observed by HR-TEM in Figure 2e. The $CeTi_2O_6$ crystal structure represented in Figure 2f belongs to the monoclinic crystal system and is built from anatase-type zigzag layers of TiO_6 octahedra sharing corners and edges in the a/b plane. The TiO_6 layers are connected along the *c* axis by corner-sharing with CeO_6 octahedra.[41,42] $CeTi_2O_6$ as well as anatase and rutile polymorphs of TiO_2 were observed as individual particles but the presence of $CeTi_2O_6$ at the CeO_2–TiO_2 interface cannot be excluded. It should be noted that the brannerite particles appear as composed of anisotropically oriented crystal domains of smaller size (ca. 2 nm) suggesting a great extent of short-range order but longer range disorder.

WO_3 and CeO_2 were never detected in the form of isolated crystalline particles in the TEM images, confirming the amorphous nature of the former one and the strong dependence of the latter one on the TiO_2 structure, as explained above. The systematic combination of CeO_2 and TiO_2 particles does not agree with previous observations on similar materials prepared by an oxygen-methane flame.[23] We associate the discrepancy with the different metal precursors and the flame conditions. Despite the experimental differences, the evident phase transformations described in the following upon increase of cerium content are identical.

The X-ray diffraction (XRD) patterns of all flame-made materials are shown in Figure 3. TiO_2 is well crystallized and

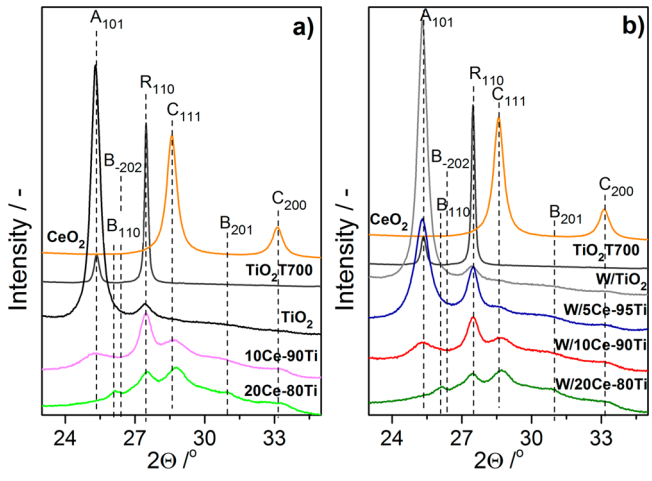

Figure 3. X-ray powder diffraction patterns of (a) 10Ce-90Ti and 20Ce-80Ti, (b) W/TiO_2, W/5Ce-95Ti, W/10Ce-90Ti and W/20Ce-80Ti compared to flame-made CeO_2, TiO_2 and TiO_2T700. A: anatase; R: rutile; C: cubic CeO_2; B: brannerite $CeTi_2O_6$.

DOI: 10.1021/acscatal.5b01580
ACS Catal. 2015, 5, 5657–5672

consists of 95 wt % anatase (ICSD 01-071-1167) and around 5 wt % rutile (ICSD 01-087-0920). Thermal treatment at 700 °C caused the anatase to rutile (A−R) transformation that is deleterious to the performance of conventional SCR catalysts.[31,43−45] The presence of tungsten oxide increased the level of background noise but did not contribute to the overall diffraction pattern indicating the good dispersion of the W-containing phase. The fraction of anatase in W/TiO_2 increased by 1 wt % at the expense of rutile (Figure 3b) as a result of the stabilization effect of the anatase structure by WO_3. The addition of cerium to TiO_2 strongly decreased the degree of crystallinity and changed especially the phase composition (Figure 3) in marked contrast to the behavior of WO_3. The presence of cerium stimulated the A−R phase transformation.

An increase of the Ce/Ti ratio caused a progressive decrease of the fraction of anatase, which practically disappears in the diffraction patterns of 20Ce-80Ti (Figure 3a) and W/20Ce-80Ti (Figure 3b). Rutile dominates the XRD pattern of 10Ce-90Ti and W/10Ce-90Ti. Other phases appeared simultaneously to the disappearance of anatase, which were identified as brannerite ($CeTi_2O_6$, ICSD 01-084-0496) and cubic fluorite CeO_2 (ICSD 03-065-5923). Although the fraction of rutile passed through a maximum in 10Ce-90Ti and W/10Ce-90Ti, the reflections of these phases intensified with increasing cerium content, suggesting a consecutive phase transformation from anatase to rutile followed by an increase of cubic CeO_2 and brannerite at the expenses of rutile. This phase transformation must be induced by cerium because the same effect is visible in both the W-free and the W-containing samples. Moreover, the weak reflections of the Ce-containing samples reveals that a strong amorphous component evidently contributes to their XRD pattern.

The A−R phase transformation induced by cerium can be accompanied by incorporation of cerium ions into the TiO_2 lattice. Ce^{4+} and Ce^{3+} have large ionic radii (IR, 87 and 101 pm, respectively) compared to Ti^{4+} (60.5 pm) in the octahedral coordination.[46] Therefore, a limited number of Ce ions can enter substitutional sites in the cationic sublattice of TiO_2. This phenomenon is demonstrated by the noticeable shift of the diffraction peaks of anatase toward lower 2Θ likely caused by lattice expansion (Figure 3). The A−R phase transformation is induced and accelerated by oxygen vacancies, which are formed as the result of charge compensation by introducing substitutional cations (e.g., Ce^{3+}) with lower valence than the host cation (Ti^{4+}).[47,48] Thus, despite the absence of any evidence in HR-TEM and XRD of the presence of Ce^{3+}-containing phases, we consider that cerium was partly incorporated into the cationic TiO_2 sublattice as a Ce^{3+} (TiO_2:Ce), according to the following equation using the Kröger−Vink notation:[49]

$$Ce_2O_3 \rightarrow 2Ce'_{Ti} + 3O_O + V_O^{\cdot\cdot} \quad (8)$$

where Ce'_{Ti} indicates Ce^{3+} on a Ti^{4+} lattice site with singular negative charge, O_O is an oxygen atom on an oxygen site, and $V_O^{\cdot\cdot}$ is an oxygen vacancy with double positive charge.

The formation and stabilization of Ce^{3+} and of the oxygen vacancies can also be realized by doping of Ti^{4+} ions into the cubic structure of CeO_2 (CeO_2:Ti), according to the following equation:[39,50]

$$2Ce_{Ce} + O_O \rightarrow 2Ce'_{Ce} + V_O^{\cdot\cdot} + \frac{1}{2}O_2\uparrow \quad (9)$$

where Ce_{Ce} is Ce^{4+} on a lattice site of ceria, O_O is an oxygen atom on an oxygen lattice site, Ce'_{Ce} indicates Ce^{3+} in the lattice site of ceria with singular negative charge, and $V_O^{\cdot\cdot}$ is an oxygen vacancy with double positive charge. The lattice contraction of cubic CeO_2 caused by such a type of doping is demonstrated by the evident shift of the of CeO_2 diffraction peaks toward higher 2Θ with increasing cerium content (Figure 3). It is known both at theoretical[39,50,51] and experimental[39,52] levels that titanium doping into the CeO_2 lattice causes formation of oxygen vacancies. Andersson et al.[50] showed using DFT calculations that substitutional doping of Ti^{4+} into the CeO_2 cationic sublattice has the largest impact on the reduction capability of the host among all investigated quaternary cations. Ti^{4+} doping of CeO_2 induced a lattice geometry relaxation due to its smaller size (IR, 74 pm) compared to Ce^{4+} (97 pm) and Ce^{3+} (114.3 pm) in coordination number 8.[46] The reduction of Ce^{4+} to larger Ce^{3+}, followed by oxygen vacancy formation, distorts the surrounding fluorite lattice, whereas the presence of small Ti^{4+} ions in the substitutional position of the cationic sublattice lowers the energetic penalty induced by lattice disorder. Dutta et al.[52] demonstrated experimentally that a short and a long oxygen bond type can be produced by the presence of Ti^{4+} in CeO_x, the latter one being weaker and responsible for the enhanced reducibility and oxygen storage capacity of CeO_2:Ti. However, because CeO_2 and TiO_2 have limited solubility due to their lattice mismatch, they do not form a solid solution. As suggested by Andersson et al.,[50] the $CeO_2−TiO_2$ solid solution can be prepared by synthesis methods allowing the formation of metastable phases. FSS is one of these methods. Metastable phases are obtained as a result of the high flame temperatures and the fast quenching.

It should be noted that all assigned crystallographic phases detected by TEM and XRD contain only Ce^{4+}. Besides the aforementioned origin of Ce^{3+} and of the associated oxygen vacancies, both types of defects can occur also in the brannerite phase, despite the formal oxidation state +4 of cerium. According to literature, $CeTi_2O_6$ is a high-temperature entropy-stabilized compound that can be unstable and decompose to the corresponding binary oxides below a critical temperature.[53] Huynh et al.[54] have found by XANES that both oxygen vacancies and Ce^{3+} are present in $CeTi_2O_6$ synthesized at high temperature and quenched. The existence of Ce^{3+} was associated with the exothermicity of its oxidation reaction and to a shift of the equilibrium toward reduced valence at high temperature, where the thermodynamic equilibrium could not be reached.

3.1.2. Chemical Composition. It is tempting to conclude from Figure 1 that flame-made catalysts have a similar morphology irrespective of composition. Conversely, distinctive differences in composition and arrangement of the elements can be clearly seen using scanning transmission electron microscopy (STEM). Figure 4 shows that the significant difference in atomic weight between Ti (Z = 22), W (74), and Ce (58) provides a clear Z-contrast allowing a more precise determination of particle composition. STEM also allows the assessment of the morphology of the tungsten component that is otherwise invisible in XRD and TEM. The dark field (DF) STEM image of TiO_2 (Figure 4a) shows homogeneous bright particles, indicating a uniform composition. In W/TiO_2, tungsten is deposited on the surface of TiO_2 in the form of a homogeneous bright layer of tungsten oxide (Figure 4b). Jossen et al.[45] arrived to the same conclusion from HR-TEM images of flame-made $V_2O_5−WO_3−TiO_2$ catalysts.

The comparison of the DF and the bright field (BF) STEM images of Figure 4c,d reveals that the clearly discernible layer of

DOI: 10.1021/acscatal.5b01580
ACS Catal. 2015, 5, 5657−5672

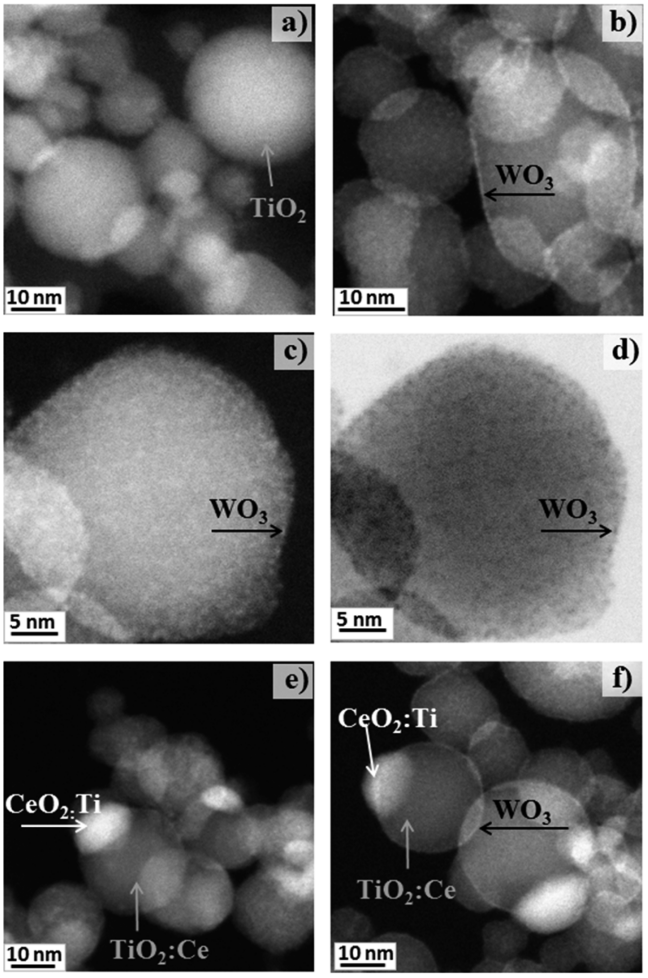

Figure 4. DF-STEM images of (a) TiO_2, (b) W/TiO_2, (e) 10Ce-90Ti, and (f) W/10Ce-90Ti. TiO_2:Ce and CeO_2:Ti particles and the WO_3 layer are indicated for clarity. (c) Enlarged DF- and (d) BF-STEM images of W/TiO_2.

WO_3 is not continuous but is present in the form of homogeneously dispersed clusters smaller than 0.5 nm. Despite the relatively high content of tungsten in the material (10 wt %), XRD is not able to detect such objects. The formation of small well-dispersed clusters is supported by the calculation of the WO_3 surface coverage (Table 1), which is based on the assumption that a full monolayer coverage of WO_3 requires 4.5 tungsten atoms·nm^{-2}.[10] Flame-made nanoparticles have intermediate WO_3 surface coverage (Table 1), in the range of 61−75% depending on the SSA value. Therefore, it can be assumed that WO_3 clusters on TiO_2 and CeO_x-TiO_2 are present in the form of WO_5 and WO_4 units of polytungstate species that are able to induce both Brønsted and Lewis acidity.[10,12] Despite the homogeneous precursor mixture used for flame synthesis, the observed WO_3 layer formation on the surface of TiO_2 and CeO_x-TiO_2 is a consequence of the low solubility of WO_3 in TiO_2[55] and of the high vapor pressure of WO_3 compared to TiO_2 and CeO_2. In V-based NH_3−SCR catalysts, the dispersion of WO_3 on the TiO_2 surface is considered to enable a better dispersion of vanadia.[1]

Addition of the cerium precursor to the precursors solution resulted in the formation of cerium-rich particles on the titanium-rich particles (Figure 4e), which can be denoted as TiO_2:Ce/CeO_2:Ti. A similar arrangement of particles was observed for W/10Ce-90Ti, where bright cerium-rich particles likely grew out of darker titanium-rich particles (Figure 4f, Figure S2) and were homogeneously coated by the bright WO_3 layer discussed for W/TiO_2 (Figure 4). Moreover, the element mapping (Figure S2c) demonstrates a very good distribution of cerium within titanium-rich particles (TiO_2:Ce) suggesting an intimate contact between cerium and titanium. This also supports our notion of the TiO_2:Ce/CeO_2:Ti indicating the presence of cubic CeO_2 particles containing Ti atoms supported on TiO_2 particles in which cerium atoms are dispersed. An increase in the Ce/Ti ratio in W/Ce−Ti caused the increase of the size of cerium-rich particles on the surface of the titanium-rich core, whose size in turn slightly decreased (Figure 5).

Nearly constant concentration of cerium (Ce K) and decreasing titanium concentration (Ti K) can be observed in the point EDS spectra of cerium rich particles (CeO_2:Ti) of Figure 5A with increasing cerium loading. The presence of titanium in cerium-rich particles proves that Ti enriched CeO_2 phases. Similarly, cerium was detected in titanium-rich particles (Figure 5B), indicating the partial incorporation of cerium into TiO_2. Unfortunately, the high scattering of cerium atoms precludes the identification of titanium in cerium-rich particles in the element mapping (Figure S2f). In contrast, the tungsten concentration remained constant for all W/Ce−Ti catalysts irrespective of the cerium concentration (Figure 5A,B), which is in agreement with the results of STEM, ICP-OES, and XPS measurements (Table 2), indicating that all tungsten is deposited as an oxide layer on the particles surface.

The nominal chemical composition of the W/Ce−Ti catalysts was confirmed by ICP-OES (Table 2, Figure 6b). The surface chemical composition was determined from XPS analysis. The surface concentrations of tungsten, cerium, and titanium are listed in Table 2.

Analysis of the W 4f and W 4d photopeaks indicates that tungsten exhibited a constant oxidation state of +6 in all investigated samples (Figure S3b). This is in agreement with the observations of Hilbrig et al.,[12] who showed that tungsten is hexavalent and anchored to the surface of TiO_2 as WO_5 and WO_4 units at low WO_x coverage (below the monolayer).

The Ce 3d region is very complex and was deconvoluted as presented in Figure 6a for 10Ce-90Ti and in Figure S4 for W/Ce−Ti samples. The spectral lines denoted as v, v″, v‴ and u, u″, u‴ are attributed to Ce^{4+}, while v_0, v′ and u_0, u′ are assigned to Ce^{3+} (Figure 6a) according to common literature practice.[56,57] Based on the intensities of the spectral lines, the concentration of Ce^{4+} was estimated according to eq 7,[58] and the results are listed in Table 2:

$$C_{Ce^{4+}} \approx \frac{I_{u'''}}{0.14\cdot(I_{v_0} + I_v + I_{v'} + I_{v''} + I_{v'''} + I_{u_0} + I_u + I_{u'} + I_{u''} + I_{u'''})} \quad (7)$$

Ce^{3+} was the only surface cerium species detected on W/5Ce-95Ti. Its concentration decreased with increasing Ce/Ti ratio reaching 80% in W/20Ce-80Ti (Table 2). A similar trend was observed by Watanabe et al.[59] who reported that the Ce^{3+} surface concentration decreased from 40% in $Ce_{0.1}Ti_{0.9}O_2$ to 15% in CeO_2. In the flame-made materials, additional cerium in the precursor solution mainly supplied the CeO_2 core but did not modify substantially the surface composition, which consisted mostly of Ce^{3+}, in agreement with the STEM results.

Ce^{3+} is considered to form in Ce−Ti-based catalysts containing only Ce^{4+} upon introduction of tungsten.[8,14] In

DOI: 10.1021/acscatal.5b01580
ACS Catal. 2015, 5, 5657−5672

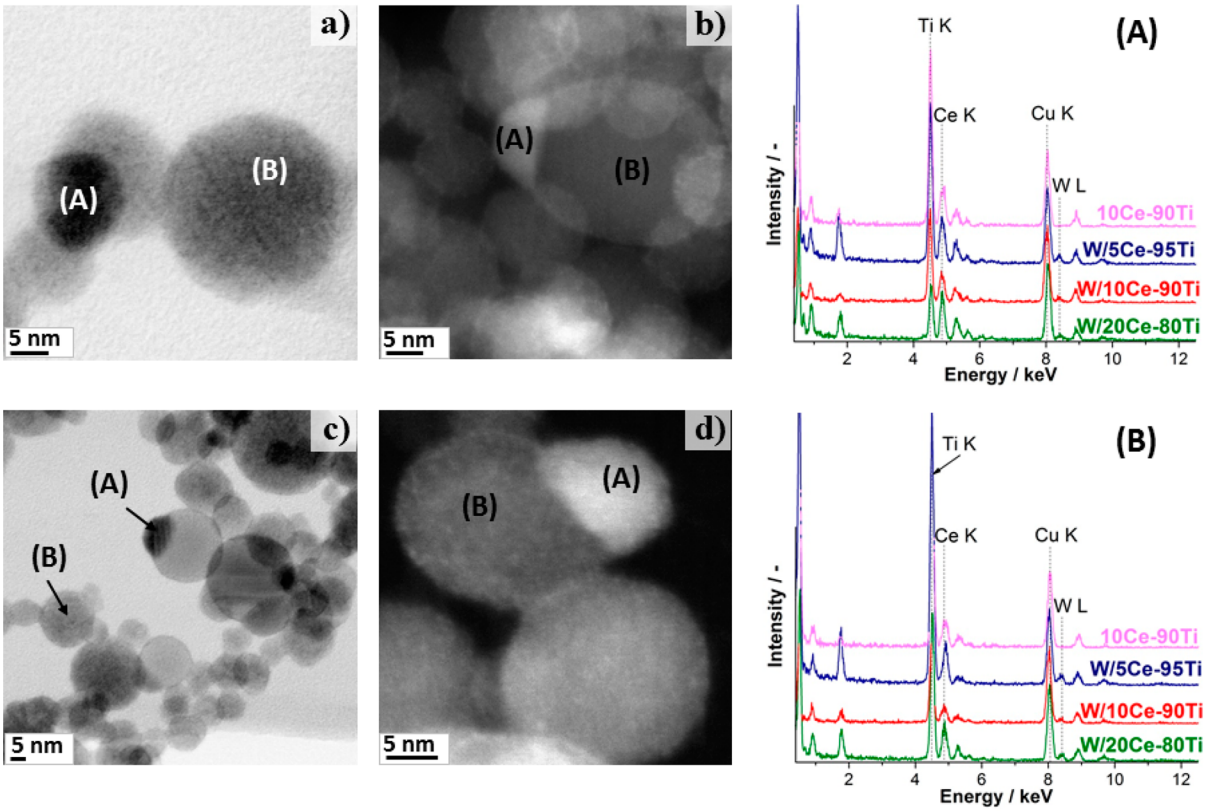

Figure 5. STEM images of (a) 10Ce-90Ti, (b) W/5Ce-95Ti, (c) W/10Ce-90Ti and (d) W/20Ce-80Ti. (A) and (B) indicate the beam positions for point EDS analysis corresponding to (A) and (B) sets of EDS spectra.

Table 2. Comparison of the Chemical Composition of Flame-Made SCR Catalysts Assessed by ICP-OES and XPS

	nominal/at.%			ICP-OES/at.%			XPS/at.%			XPS/%
sample name	Ti	W	Ce	Ti	W	Ce	Ti^{4+}	W^{6+}	Ce	Ce^{3+}
V–W/Ti	94.0	3.7	2.3[a]	–	–	–	–	–	–	–
TiO_2	100	–	–	–	–	–	100	–	–	–
W/TiO_2	96.3	3.7	–	–	–	–	90.2	9.8	–	–
10Ce-90Ti	90	–	10	–	–	–	85.5	–	14.5	83
20Ce-80Ti	80	–	20	–	–	–		–	–	–
W/5Ce-95Ti	91.3	3.9	4.8	90.5	3.9	5.6	81.2	9.4	9.4	100
W/10Ce-90Ti	86.3	4.1	9.6	85.2	4.1	10.7	74.2	10.4	15.4	86
W/20Ce-80Ti	76.4	4.5	19.1	74.8	4.3	20.9	69.6	10.2	20.2	80

[a]Concentration of V/at.%

our flame-made materials, the amount of Ce^{3+} was already high (above 80%) and changed only slightly upon the introduction of tungsten in W/10Ce-90Ti. We relate this discrepancy of Ce oxidation state to the difference in the synthesis. Chen et al.[8,14] prepared the mixed oxide catalyst by coimpregnation of TiO_2 with cerium and tungsten precursors ensuring the formation of the CeO_2–WO_3 interaction but not the strong interaction of these oxides with TiO_2. In contrast, in this work Ce-, W-, and Ti-precursors were homogeneously mixed and sprayed into the flame simultaneously, allowing close interaction between each component. This can affect their oxidation state. As a result, Ce^{3+} is the dominant surface cerium species in the flame-made catalysts and is considered crucial from the NH_3–SCR perspective.[8,14] Figure 6b demonstrates that the W/Ce+Ti ratio of all investigated samples obtained from XPS analysis is similar and 2.5 times higher than that obtained from ICP-OES. Therefore, all tungsten is dispersed on the surface of flame-made catalysts irrespective of the overall chemical composition of the materials, in perfect agreement with the STEM and EDS investigations.

The Ce/Ti ratio measured by XPS was always higher than that obtained by ICP-OES. The cerium content of W/5Ce-95Ti measured by XPS was 1.7 times higher than that measured with ICP-OES and decreased with increasing cerium content reaching 1 for W/20Ce-80Ti. The discrepancy between the two measurements arises most likely from the enrichment of the surface by cerium, which can be evaluated more accurately by the surface sensitive XPS (penetration depth ~10 nm for metal oxides) rather than by bulk methods. The surface enrichment corresponds also well with the STEM observations (Figure 5) and the element mapping (Figure S2). Therefore, the chemical composition of the surface becomes increasingly homogeneous with increasing cerium content. Furthermore, the additional cerium added from sample to sample occupies bulk position

DOI: 10.1021/acscatal.5b01580
ACS Catal. 2015, 5, 5657–5672

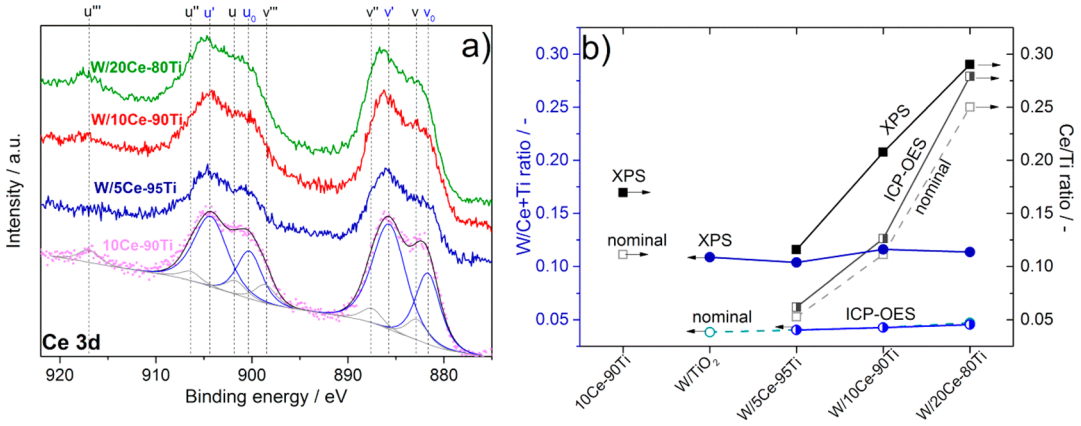

Figure 6. (a) Ce 3d photoelectron spectra of W/20Ce-80Ti, W/10Ce-90Ti, W/5Ce-95Ti, and 10Ce-90Ti with exemplary spectrum deconvolution and indicated spectral lines. (b) W/Ce+Ti and Ce/Ti ratios for WO_3/CeO_x-TiO_2 catalysts obtained from nominal value, ICP-OES, and XPS analysis.

rather than surface position, which explains the tendency of XPS data against ICP-OES data, the decreasing fraction of Ce^{3+} and the increasing size of the ceria particles with increasing cerium content.

Complementary to XPS, the cerium oxidation state in the flame-made catalysts was examined by X-ray absorption near edge spectroscopy (XANES). The Ce L_3-edge XANES spectrum of $Ce(NO_3)_3$, taken as the Ce^{3+} reference significantly differs from that of the Ce^{4+} reference (CeO_2, Figure 7).[60,61] In

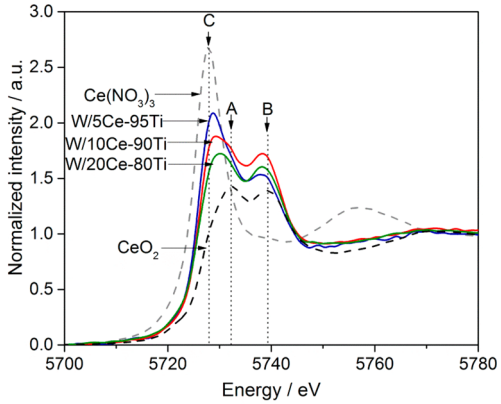

Figure 7. Normalized Ce L_3-edge XANES spectra of flame-made catalysts, Ce^{3+} ($Ce(NO_3)_3$, peak C) and Ce^{4+} (CeO_2, peaks A and B) references.

the former, the characteristic white line (indicated as C) corresponds to the $2p_{2/3} \rightarrow (4f^1)5d$ electronic transition. In CeO_2, the two characteristic features separated by around 7 eV (A and B) correspond to $2p_{2/3} \rightarrow (4fL)5d$ and $2p_{2/3} \rightarrow (4f^0)5d$ electronic transitions.[62,63] Figure 7 demonstrates that the oxidation state of flame-made catalysts lies between those of the references indicating mixed oxidation state. The fraction of Ce^{4+} increased with increasing cerium concentration in agreement with the XPS data of Table 2 (Figure S5). We consider that the size of the CeO_2:Ti particles on TiO_2:Ce increases with increasing cerium concentration (Figure 3 and Figure 5), and the fraction of Ce^{4+} in the bulk increases accordingly.

Furthermore, the presence of tungsten on the catalyst surface increased the Ce^{3+} content as it was revealed by XPS studies (Table 2) and confirmed by XANES measurements (Figure S6). It was not possible to quantify the content of Ce^{3+} and Ce^{4+} in the flame-made catalysts on the basis of their Ce L_3-edge XANES spectra and the spectra of the references, as explained in detail in SI. Nevertheless, some conclusions about the Ce^{3+} content could be derived. The trend observed by XANES resembles the one obtained by XPS, but the Ce^{3+} content is noticeably lower than the one measured by XPS (Table 2). This discrepancy needs to be associated again with the surface sensitivity of XPS and the bulk sensitivity of XANES. Moreover, samples during XPS measurements were subjected to the vacuum, which might induce some reduction of the surface species. However, reduction of species other than cerium surface species was not detected by XPS. Both tungsten and titanium were on their highest oxidation states 6+ and 4+, respectively (Figure S3). Therefore, we believe that the effect of vacuum on the reduction of cerium was negligible in XPS. The XANES spectra of flame-made catalysts measured under ambient conditions demonstrate the high concentration of Ce^{3+}.

3.1.3. Acidity. Acidity is a key property of SCR catalysts because it is a prerequisite for efficient NH_3 adsorption. Therefore, the acidity of the flame-made catalysts was evaluated from ammonia temperature-programmed desorption (NH_3-TPD) measurements, whereas the nature of the acid sites was qualitatively evaluated by infrared spectroscopy using ammonia adsorption. NH_3-TPD provides a quantitative measure of ammonia uptake by the catalyst (Table 1) and a qualitative measure of the strength of acid sites. Figure 8 shows the NH_3-TPD profiles of all catalysts. All NH_3 desorption profiles extend over a broad temperature region, suggesting that they are the result of desorption from sites with different acidity strength. For the ease of discussion, we have divided the desorption profiles in four regions. Region I covers the range 50−125 °C and is assigned to physisorbed ammonia. Region II, which can be defined from 125−200 °C, is assigned to the presence of weak acid sites. The 200−350 °C temperature regime can be defined as region III and assigned to acid sites of intermediate strength. Finally, strong acid sites that release ammonia above 350 °C characterize region IV. It can be assumed that the acid sites defined in the regions II and III are important in the SCR process because activity develops in this temperature range (see section 3.2). TiO_2 exhibited a broad NH_3 desorption profile ranging from 50 to 450 °C with maximum at ca. 370 °C (Figure 8) and high ammonia uptake, which further increased in the

DOI: 10.1021/acscatal.5b01580
ACS Catal. 2015, 5, 5657−5672

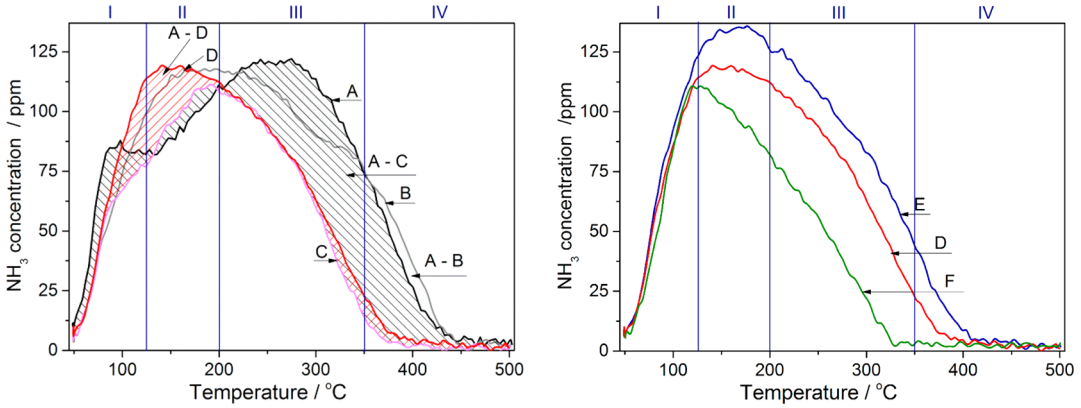

Figure 8. NH_3-TPD profiles of (A) TiO_2, (B) W/TiO_2, (C) 10Ce-90Ti, (D) W/10Ce-90Ti, (E) W/5Ce-95Ti, and (F) W/20Ce-80Ti. Shaded areas A - B (gray), A - C (black right diagonal lines) A - D (red left diagonal lines) correspond to the differences between A and B, C, or D profiles, respectively. Latin numbers indicate regions described in the main text.

presence of WO_3 (Table 1). The formation of acid sites releasing NH_3 in region II is a major characteristic of the addition of tungsten with the consequent shift of the maximum NH_3 desorption to ca. 200 °C. Therefore, tungsten induces a significant increase in the fraction of weak acid sites. Additionally, WO_3 also slightly extended the desorption peak toward high temperature compared to TiO_2. Desorption with maximum at ca. 350 °C can be assigned to acid sites with intermediate strength.

The reinforcement of the amount of acid sites by polytungstate species caused by a WO_3 surface coverage below one monolayer[10,31] is in agreement with the extent of WO_3 coverage of the investigated catalysts, which is in the range 2.8−3.4 tungsten atoms·nm^{-2} (Table 1). Contrary to tungsten, the addition of cerium to TiO_2 greatly decreased the amount of strong acid sites (region IV) and only slightly increased the amount of weak acid sites (A - C (black right diagonal lines) in Figure 8; region II). As a result, the maximum NH_3 desorption was observed at ca. 200 °C. The NH_3 uptake was reduced by 31% compared to TiO_2 suggesting that the native acidity of flame-made TiO_2 was partly suppressed by titration with cerium. Figure 8 and Table 1 show that a further increase of the cerium content to 10 and 20 mol % gradually decreased the number of high-temperature acid sites and the NH_3 uptake.

The increase of the fraction of weak acid sites upon addition of cerium can be associated with the high surface concentration of Ce^{3+} measured by XPS, which is considered to contribute to the SCR activity as Brønsted acid site.[8] Watanabe et al.[59] investigated $Ce_xTi_{1-x}O_2$ with $0 < x < 1$ and reported that the increase of cerium content in TiO_2 decreases the amount of both weak and strong Lewis acid sites. The most significant increase of weak acid sites was observed for $Ce_{0.1}Ti_{0.9}O_2$, which exhibited also the highest content of surface Ce^{3+} and demonstrated the highest NH_3 oxidation activity.[59]

The shape of the NH_3 desorption profiles of W/Ce−Ti can be considered as the result of the overlap between the effects of cerium and tungsten on TiO_2 (Figure 8, A - D (red left diagonal lines)).

The nature of the NH_3 adsorption sites induced by the addition of cerium and tungsten to TiO_2 was determined using diffuse reflectance Fourier transform infrared (DRIFT) spectroscopy. Figure 9 shows the DRIFT spectra in the spectral range 2100−950 cm^{-1} that were collected when passing 500 ppm of NH_3 at 50 °C on TiO_2, W/TiO_2, 10Ce-90Ti, and W/10Ce-90Ti. At 50 °C, NH_3 coordinates on various Lewis acid sites of TiO_2 as indicated by the signals at 1601, ca. 1245 and 1165 cm^{-1} (Figure 9b).[64] Signals at 1650 and around 1400 cm^{-1} show little contribution of Brønsted acid sites, which are unusual for TiO_2 especially in the absence of sulfate species. However, these sites may arise from the nature of flame-made TiO_2. Due to the fact that the experimental conditions of FSS do not allow the particles to reach thermodynamic equilibrium, the surface is highly defective as demonstrated by the round shaped TiO_2 particles visible in the TEM/STEM images.

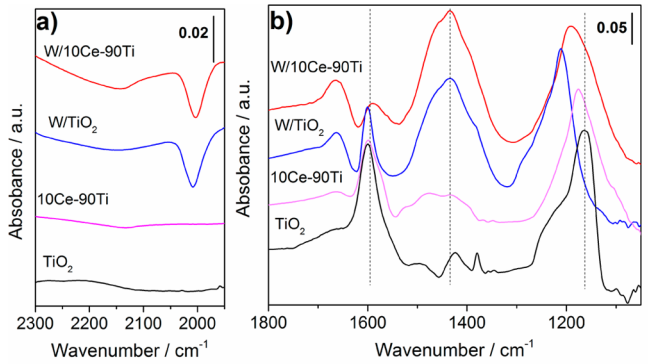

Figure 9. In situ DRIFT spectra of NH_3 adsorption at 50 °C on TiO_2, W/TiO_2, 10Ce-90Ti, and W/10Ce-90Ti in the spectral ranges (a) 2300−1950 cm^{-1} and (b) 1800−1050 cm^{-1}. The vertical lines are used to guide the eye.

Cerium generates Brønsted acidity likely of the type Ce^{3+}−O−Ti^{4+} as indicated by the broad feature centered at 1432 cm^{-1} in 10Ce-90Ti. The new shoulder below 1600 cm^{-1} and the different shape of the signal at ca. 1200 cm^{-1} suggest also changes in the environment of the Lewis acid sites. These changes remain upon addition of tungsten. The blue shift of the latter signal from TiO_2 to 10Ce-90Ti and even more in the case of W/10Ce-90Ti can be partly ascribed to the phase changes observed from XRD. The Ce-containing materials contain rutile, on which the symmetric N−H deformation mode of coordinated NH_3 appears systematically at higher energy than in the corresponding spectra on anatase.[65] The major improvement obtained with tungsten is the considerable increase of the fraction of NH_4^+ coordinated to Brønsted acid sites,[1] which reflects in the appearance of signals at 1680 and 1432 cm^{-1} for 10Ce-90Ti and 1664 and 1432 cm^{-1} for W/

DOI: 10.1021/acscatal.5b01580
ACS Catal. 2015, 5, 5657−5672

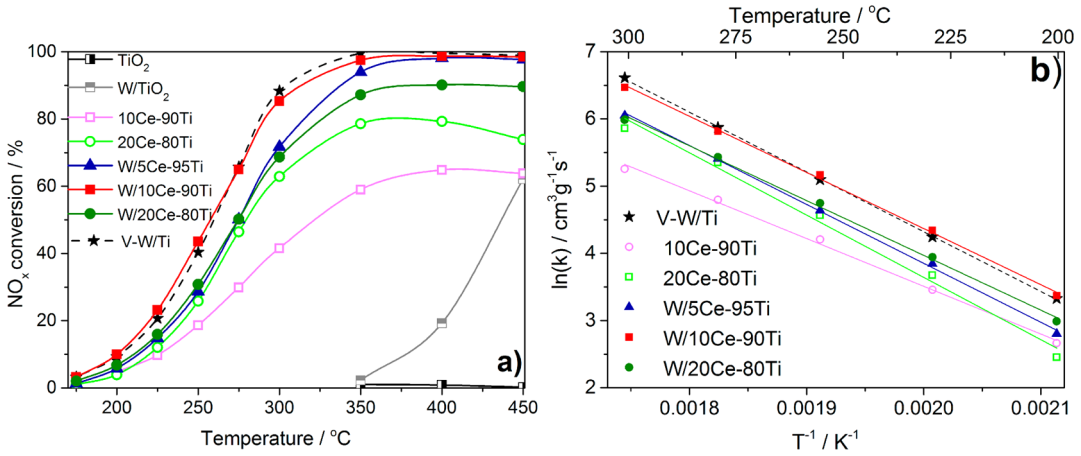

Figure 10. (a) NO_x conversion over flame-made catalysts as a function of temperature at GHSV = 600 $L \cdot g^{-1} \cdot h^{-1}$ and (b) Arrhenius plots. The V–W/Ti reference catalyst is 2.4 wt % V_2O_5-10 wt % WO_3/ TiO_2 prepared by wet impregnation.[2]

10Ce-90Ti. The coordinatively adsorbed NH_3 on Lewis acid sites is very different in W/TiO_2 compared to the other samples. The low frequency signal observed in TiO_2 at 1165 cm^{-1} vanishes completely, while the shoulder at ca. 1245 cm^{-1} in TiO_2 becomes the dominant signal and extends to 1300 cm^{-1} in W/TiO_2. The shift to high frequency of the N–H deformation mode in W/TiO_2 in general suggests that these sites are weaker compared to Lewis acid sites of TiO_2. The shift is evident only for the N–H deformation mode because this is more sensitive to the adsorption environment than the stretching mode (ca. 1600 cm^{-1}). However, on the basis of the substantial variation of the spectral features between TiO_2 and W/TiO_2, we propose that the new signals characterize new type of acid sites compared to TiO_2 and that these must correspond only to Lewis acid sites having tungsten as the coordination center. Therefore, the spectra of Figure 9 confirm that tungsten covers TiO_2 but also that acidity of W/TiO_2 is provided primarily by tungsten.

The new Lewis acid sites obtained with tungsten become a minority species in the presence of cerium in W/10Ce-90Ti. Conversely, the TiO_2 Lewis sites remain. This agrees well with the STEM observation showing that, contrary to conventional preparations of SCR catalysts, tungsten covers the other two components rather than only TiO_2. In our opinion, the difference between the spectra of W/TiO_2 and W/10Ce-90Ti suggests that the Lewis acidity is in nature similar to that found on TiO_2, whereas the Brønsted acidity originates from the Ce–W contact. The observation that reduced ceria possesses a larger fraction of Brønsted acid sites than pristine ceria[4] prompts us to think that these sites involve Ce^{3+}, the dominant cerium surface species, and are thus of the type Ce^{3+}–O–W^{6+}.

The presence of tungsten and cerium in the spectra is manifested in the spectral region 2300–1950 cm^{-1} (Figure 9a). The negative signal at 2003 cm^{-1} corresponds to the first overtone (2ν(W═O)) of surface wolframyl species and is accompanied by a strong negative signal at 1003 cm^{-1}, the fundamental W═O mode (not shown).[66] Tungsten also increased the overall surface Brønsted acidity as suggested by a higher signal intensity of adsorbed NH_3 species in agreement with the evident larger NH_3 uptake in Table 1. On the other hand, the presence of cerium reflects in the negative signal at ca. 2150 cm^{-1} that is visible upon coordination with NH_3 in the ternary catalyst (Figure 9a). The energy of this signal matches well with consumption of and thus the coordination of NH_3 to Ce^{3+} centers.[67] The weak feature corresponding to the cerium component in the case of the binary catalyst may reveal the promotion of tungsten to NH_3 coordination in the close vicinity of cerium centers. This again confirms that the component primarily responsible for acidity in 10Ce-90Ti is TiO_2, whereas the above-mentioned Ce–O–W species generated by the close contact of cerium and tungsten may represent the reactive adsorption sites for NH_3 in W/10Ce-90Ti.

3.2. Catalytic Activity and Aging. Figure 10a presents the catalytic activity data for NH_3–SCR obtained on the various materials. The samples are compared with a conventional SCR catalyst based on vanadium (V–W/Ti, 2.4 wt % V_2O_5/ 10 wt % WO_3/ TiO_2).[2] Comparison with a Ce–W–Ti based catalyst prepared by sequential impregnation of TiO_2 with cerium and tungsten was reported previously.[30]

Addition of cerium to TiO_2 induced SCR activity in a wide temperature window from 200 to 450 °C, confirming that cerium is a crucial SCR-active component. Increasing the cerium content to 20 mol % resulted in improved NO_x conversion reaching 79% at 400 °C. On the contrary, the addition of WO_3 to TiO_2 induced only high-temperature activity (>350 °C) with a maximum NO_x conversion of 62% at 450 °C. The addition of WO_x to CeO_x-TiO_2 increased the overall catalytic performance and W/10Ce-90Ti was the most active catalyst in the series. The performance of W/10Ce-90Ti was comparable to that of V–W/Ti. The activity data demonstrate the important role of tungsten in the SCR catalysis[8,13,14] and that both cerium and tungsten are required for high SCR activity. However, an optimum cerium content is required because both an increase (20 at. %) and a decrease (5 at. %) of the cerium loading negatively affected the NO_x conversion.

The reaction rate constants (k) were calculated from eq 6 for the catalysts tested at GHSV = 600 $L \cdot g^{-1} \cdot h^{-1}$ in the 200–300 °C temperature range (Figure 10b). Under the assumption that the reaction mechanism on Ce–W–Ti catalysts is equivalent to that generally accepted for V-based catalysts, in this temperature range and under excess of NH_3 (α = NH_3/NO = 1.2), it can be assumed that NH_3 fully covers the catalyst surface fulfilling the zeroth order requirement with respect to NH_3.[36,37] The values of k at 200 °C together with the apparent activation energies calculated from the slope of the Arrhenius plots are listed in Table 3. Among the flame-made catalysts, 10Ce-90Ti

DOI: 10.1021/acscatal.5b01580
ACS Catal. 2015, 5, 5657–5672

Table 3. Reaction Rate Constants (k) Determined at 200 °C and GHSV = 600 L·g^{-1}· h^{-1} and Apparent Activation Energy (E_a) for the Investigated Catalysts

	V−W/Ti	10Ce-90Ti	20Ce-80Ti	W/5Ce-95Ti	W/10Ce-90Ti	W/20Ce-80Ti
k/cm^3·g^{-1}· s^{-1} at 200 °C	27.9	14.4	11.6	16.5	29.1	19.8
E_a / kJ·mol^{-1}	73.9	59.1	77.1	72.9	69.4	72.9

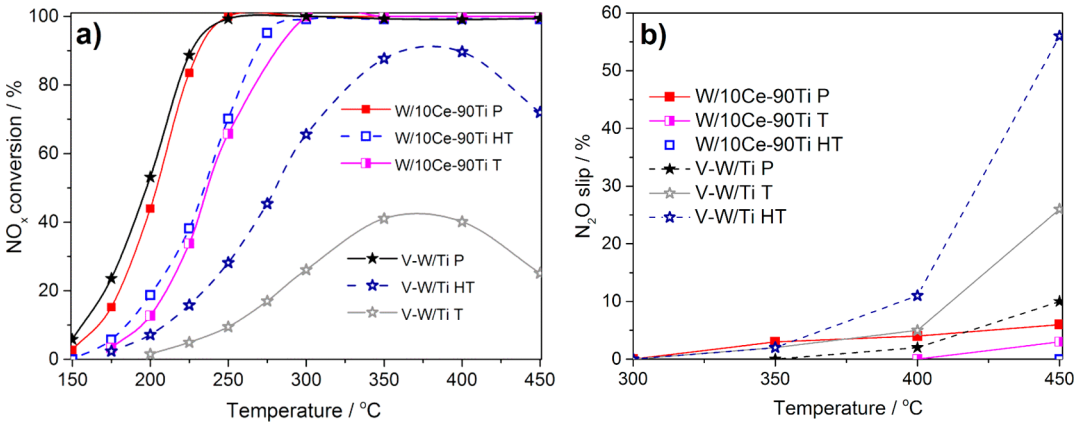

Figure 11. (a) NO_x conversion and (b) N_2O slip over fresh and aged W/10Ce-90Ti and V−W/Ti catalysts. P: as-prepared; T: after thermal aging; HT: after hydrothermal aging. Conditions: GHSV = 120 L·g^{-1}· h^{-1}; feed: 1000 ppm of NO, 1200 ppm of NH_3 in 10 vol % O_2, 5 vol % H_2O in N_2.

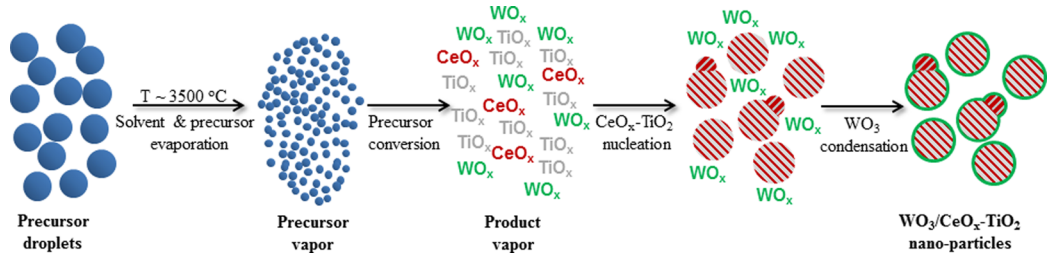

Figure 12. Schematic representation of a feasible mechanism of WO_3/CeO_x-TiO_2 nanoparticles formation during FSS.

showed the lowest activation energy barrier but also the lowest reaction rate constant and therefore low deNO_x performance. The addition of WO_3 resulted in the increase in the reaction rate constant. Among ternary catalysts, including V−W/Ti, W/10Ce-90Ti exhibited the lowest activation energy barrier and the highest reaction rate constant. Therefore, this material demonstrated a better performance than the V−W/Ti catalyst. Furthermore, W/10Ce-90Ti was characterized by the lowest NH_3 slip (Figure S7a) and by low levels of N_2O (Figure S7b).

The SCR activity of W/10Ce-90Ti and V−W/Ti was further evaluated after thermal (T) and hydrothermal (HT) aging at 700 °C for 15 h (Figure 11). Both types of aging protocols affected the NO_x conversion of the aged catalysts. V−W/Ti is known to suffer from low thermal and hydrothermal stability because of the A−R transformation and the sintering of WO_3.[2] The poor resistance of V−W/Ti against aging at high temperature is confirmed by the measurements of Figure 11 showing that treatment at 700 °C significantly decreases the overall activity, thermal aging being more severe than hydrothermal aging. This temperature is rather high for SCR catalysts. The NO_x conversion of V−W/Ti dropped to 41% at 350 °C after thermal treatment (Figure 11a) and was accompanied by the formation of N_2O ranging from 12 ppm at 450 °C for the as-prepared catalyst to 26 ppm after thermal treatment (Figure 11b).

Similarly, V−W/Ti reached 89% of NO_x conversion at 400 °C with 56 ppm of N_2O at 450 °C after hydrothermal treatment. In marked contrast, W/10Ce-90Ti exhibited still full conversion in the 300−450 °C range after thermal and hydrothermal treatments. The N_2 selectivity improved after aging and only 3 ppm of N_2O were measured at 450 °C for W/10Ce-90Ti-T, while no N_2O was detected in the case W/10Ce-90Ti-HT. Aging had a large effect on the low temperature activity of W/10Ce-90Ti, but W/10Ce-90Ti-HT still exhibited 70% NO_x conversion at 250 °C compared to 30% of V−W/Ti-HT.

We anticipate that the XPS data of the aged samples indicate that the fraction of Ce^{3+} decreased from 83% to 58% after thermal aging (W/10Ce-90Ti-T) and to 63% in the case of hydrothermal aging (W/10Ce-90Ti-HT). Hence, a considerable fraction of cerium is still in the oxidation state +3 after high-temperature exposure even in the presence of water. A detailed description of structural changes occurring upon aging will be reported in a forthcoming publication.

3.3. Particle Formation and Structure−Activity Relationship. The most active catalyst produced in this work, W/10Ce-90Ti, is composed of cerium-doped rutile particles (TiO_2:Ce) in contact with titanium-doped cubic ceria particles (CeO_2:Ti), isolated brannerite particles, and in minority cerium-doped anatase TiO_2. Additionally, these phases coexist with amorphous Ce−Ti mixed oxides, while tungsten oxide and Ce^{3+} species homogeneously cover these structures. Hence, both the arrangement of the elements and the phase composition of this material are unique. We have shown that

DOI: 10.1021/acscatal.5b01580
ACS Catal. 2015, 5, 5657−5672

this unusual structure cannot be easily reproduced (e.g., using conventional wet impregnation)[30] and that it generates a very active and aging resistant catalyst for NH_3−SCR (Figures 10 and 11). The peculiar morphology, composition, and arrangement of elements of the flame-made WO_3/CeO_x-TiO_2 catalyst originate from the nature of the oxygen-acetylene flame used for synthesis. High flame temperatures (~3800 K) and the short residence time (5 ms) of the particles formed in the flame followed by a fast quenching (~500 000 K/s) allows the freezing of metastable phases not accessible otherwise (i.e., using conventional synthesis methods). The formation of materials in the flame is not governed by thermodynamics but is kinetically driven. Therefore, it was possible to obtain crystalline titanium-doped CeO_2 (CeO_2:Ti) as well as cerium-doped TiO_2 (TiO_2:Ce) along with the formation of the brannerite phase. The formation of rutile TiO_2 particles associated with the ceria particles is likely a result of the peculiar synthesis conditions as well.

Figure 12 depicts our interpretation of the mechanism of particle formation during FSS in the case of spraying of a precursor solution containing organometallics of cerium, tungsten, and titanium. After spraying the precursor solution in the form of finely dispersed aerosol in the flame, the solution and the solvent are instantly vaporized. Then, the mixed CeO_2−TiO_2 and TiO_2 phases start to nucleate due to their high melting point. In the presence of the large amount of water present in the flame as major combustion product,[68] the tungsten easily forms hydroxo species that are more volatile than the other elements. Therefore, tungsten is still present as vapor when TiO_2 and mixed CeO_x-TiO_2 already solidified. Tungsten oxide starts to condense on the surface of the Ti- and Ce-containing solid particles only in the colder zone of the flame, thus producing the homogeneous amorphous layer clearly observed by STEM.

The brannerite phase ($CeTi_2O_6$) is likely formed due to the very high temperatures in the flame and is stabilized by the fast quenching. The amount of this phase increases with increasing cerium content. It can be located at the interface of TiO_2:Ce and CeO_2:Ti or can form isolated nanoparticles (Figure 2e). The fast quenching can induce oxygen deficiency and formation of Ce^{3+}. The Ce/Ti ratio in the brannerite phase is 0.5, thus larger than in the investigated materials where it ranges from 0.05 in W/5Ce-95Ti to 0.25 in W/20Ce-80Ti. This suggests that the brannerite phase can only be formed locally where the Ce/Ti ratio is appropriate. Alternately, the brannerite phase could have formed in the flame directly from Ce and Ti precursors then gradually transforming into cerium- and titanium-rich particles by segregation of TiO_2 and CeO_2 upon traveling along the flame. We favor the first scenario based on the following observation. The XRD data of Figure 3 clearly show a sort of consecutive phase transformation where anatase is forced to transform into rutile by the presence of cerium. With increasing cerium content, the fraction of rutile passes through a maximum at 10 mol % cerium, while the contribution of cubic ceria and of the amorphous phase intensify after the maximum. Finally, brannerite is also clearly observed at 20 mol % cerium and is the last crystalline phase to appear in the XRD patterns at increasing cerium content. We think that the existence of the brannerite phase essentially represents the evidence that a close interaction between cerium and titanium occurs in these materials. This interaction exists already at low cerium content where brannerite is not yet visible (by XRD). Brannerite may represent the end of a crystallization process induced by the progressive addition of cerium to titanium. The drop of crystallinity as soon as cerium is added to the precursors followed by complete loss of anatase and increase of a smaller fraction of rutile suggests that the Ce−Ti interaction and the good mixing of the two precursors act as a seed for the formation of mixed CeO_2−TiO_2 particles. As indicated above, these particles may be of the type CeO_2:Ti and TiO_2:Ce, but their degree of crystallinity is low because of the presence of the Ce^{3+} dopant. The decrease in the fraction of rutile after 10 mol % cerium suggests that cerium does not further add to TiO_2, indicating a sort of solubility limit of Ce^{3+} in titania. At the same time, CeO_2:Ti grew on TiO_2:Ce as proven by STEM, EDS, element mapping, and XRD. The titanium and cerium dopants introduced into the CeO_2 and TiO_2 phases, respectively induced the formation of oxygen vacancies thus stabilizing Ce^{3+}.[59] As a result of the homogeneous mixing of the cerium and titanium precursors sprayed in the flame and of their comparable melting point, the final product of the synthesis contains cerium atoms well dispersed over all the material and CeO_2 particles localized on rutile. This structure entails a high portion of amorphous Ce−Ti mixed oxide phases that can be taken as an evidence of increased Ce−Ti interaction and exists because of the poor solubility of cerium in titanium. This amorphous phase is considered beneficial for catalytic performance.[17]

The presence of several crystalline phases in W/10Ce-90Ti coexisting with a fraction of amorphous phase of mixed Ce−Ti nature, well-dispersed Ce^{3+} species and the homogeneously distributed WO_3 phase makes it difficult to provide a full understanding of the excellent performance of the W/10Ce-90Ti catalyst. However, a short rationale of the role of each component can be tentatively given. In respect of its traditional role of proven metal oxide support for NH_3−SCR, titanium is the dominant element. However, the major titanium containing phase in the active catalyst is not anatase but rutile, which is contrary to common knowledge.[69] The selective production of rutile at the expenses of anatase in the presence of cerium appears a peculiarity of FSS.[23] The presence of rutile, or better formulated, the absence of anatase does not make this catalyst inactive. In view of aging characteristics, this property is even providential because rutile is the high-temperature polymorph of titania, thus no further transformation is expected except for an increase of crystallinity upon treatment at high temperature (>600−650 °C). The titania support of W/10Ce-90Ti provides Lewis acid sites, whose environment is changed compared to the Lewis acid sites of anatase. This can be the result of the presence of rutile instead of anatase and therefore the result of the presence of cerium. Finally, titania contributes to the stabilization of Ce^{3+} and oxygen vacancies.[59,70,71]

Tungsten is typically added to V-based catalysts to stabilize anatase against phase transformation, particle growth, and to induce Brønsted acidity.[1] The latter role is maintained in the flame-made materials and is crucial in W/10Ce-90Ti, while stabilization of anatase against rutile is observed only in W/TiO_2. The calculated surface coverage of tungsten remains within the values required for active SCR catalysts and confirms the very good dispersion of tungsten. The peculiar aspect of the WO_3 submonolayer in W/10Ce-90Ti (i.e., the fact that it covers both cerium and titanium components) is also not the classic one since usually tungsten is applied directly to TiO_2 prior to the vanadium phase. The arrangement obtained by FSS does not protect titanium from rutile formation. Nevertheless, this does not seem necessary for flame-made W/10Ce-90Ti,

DOI: 10.1021/acscatal.5b01580
ACS Catal. 2015, 5, 5657−5672

where rutile dominates over anatase. Tungsten generates a large fraction of weak acid sites (NH_3-TPD) and of Brønsted acid sites (DRIFT) that are probably of the type $Ce^{3+}-O-W^{6+}$, which is the reason for its good dispersion. It is likely through this close interaction that tungsten stabilizes Ce^{3+}.[14] The coverage of the cerium component by WO_3 appears crucial to suppress NH_3 oxidation activity that the Ce^{4+} species of the CeO_2 particles may intrinsically induce. Therefore, tungsten is a crucial element for the selectivity of W/20Ce-80Ti. This is demonstrated by the high NH_3 oxidation activity of 20Ce-80Ti (Figure S9), the W-free analogue of W/10Ce-90Ti that contains the highest concentration of Ce^{4+} species. This oxidation activity drops in the presence of tungsten.

The last component to discuss is cerium. The stabilization of Ce^{3+} by both titanium and tungsten and the high surface concentration of Ce^{3+} together with the high activity of W/10Ce-90Ti for NH_3–SCR indicate that this species must be associated with the intrinsic redox potential of the catalyst and thus with the $deNO_x$ activity. This is also supported by the fact that binary Ce–Ti catalysts already possess activity. The catalytic performance of W/10Ce-90Ti could be related to an optimal balance between the content of exposed Ce^{3+} and the amount of Ce^{4+} or the total cerium loading that is not attained with 5 or 20 mol % cerium. The characterization data point to the existence of Ce^{3+} species at the interface with the tungsten and the titanium components. We consider the resulting Ce–O–W and Ce–O–Ti environments crucial for the overall performance of flame-made W/10Ce-90Ti because highly dispersed tungsten and cerium species are typically associated with improved catalytic performance,[14,20] though the nature of these species may not be identical to that obtained with conventional synthesis methods.

Cerium entails also structural effects. It is clear that it induces defects in the titania structure, which have as a consequence the formation of rutile as the dominant titanium-containing crystal phase. NH_3 adsorption reveals that cerium already imparts weak Brønsted acidity to titania. Because 10Ce-90Ti is active for NH_3–SCR, this acidity is beneficial.

The expected resistance to high temperature induced by the presence of rutile is proven by the excellent aging performance compared to the V-based catalyst (Figure 11). The most important piece of information with respect to the role of the well-dispersed Ce^{3+} species is that the high-temperature treatment (700 °C) is not able to suppress it. Therefore, in the absence of any in situ/operando evidence, we consider these species the crucial component obtained by FSS. The combination and peculiar arrangement of the various elements that we have demonstrated here contribute to enhance the fraction of Ce^{3+} in the most active catalyst and to minimize the components that could provide undesired oxidation of the reactants. The homogeneous dispersion of tungsten and its close interaction with cerium and titanium surface species achieved by flame-spray synthesis is beneficial for the NH_3–SCR performance, in agreement with similar characteristics of analogue catalyst compositions displaying different arrangement of the components.[8,13,14]

4. CONCLUSION

WO_3/CeO_x-TiO_2 catalysts prepared by flame-spray synthesis using an oxygen-acetylene flame demonstrated high NO_x reduction efficiency in the selective catalytic reduction of NO_x by NH_3. The excellent catalytic activity, manifested in form of low activation energies and high reaction rates in comparison to a $V_2O_5-WO_3/TiO_2$ catalyst, can be associated with the peculiar morphology, structure, and spatial arrangement of the elements, which resulted from the synthesis technique.

In contrast to conventional preparation of similar catalyst formulations, flame-spray synthesis produced a unique ternary W–Ce–Ti catalyst. Similar to its function to disperse the active vanadium species in V–W/Ti based catalysts, the presence of TiO_2 and the interaction with cerium at the atomic level proved to be the key points for good SCR performance. The close interaction of cerium and titanium results in the formation of Ce-doped TiO_2, Ti-doped CeO_2, and $CeTi_2O_6$, followed by evolution of oxygen vacancies and a large fraction of surface Ce^{3+}, which is a crucial tile for NH_3–SCR. The poor crystallinity of the ternary samples is also an indication of the good mixing of cerium and titanium and appears crucial to enhance the fraction of surface Ce^{3+}. The homogeneous dispersion of WO_3 on the surface of the catalyst is a further key factor for the high SCR performance and reduced NH_3 oxidation activity. Amorphous WO_3 clusters were found to be homogeneously distributed on the surface of all particles. WO_3 not only improved the surface acidity and thus catalytic performance but was also responsible to further increase the fraction of Ce^{3+} by establishing a close Ce–O–W interaction. Beside morphology and relative element arrangement, the close Ce–O–W and Ce–O–Ti interactions are essential for the catalytic properties of this catalyst.

As a consequence of its structure, 10 wt % WO_3/10 mol % CeO_x-90 mol % TiO_2 exhibited the best NH_3–SCR catalytic performance, which was comparable to that of a V-based catalyst (2.4 wt % V_2O_5-10 wt % WO_3/TiO_2). The excellent performance is ascribed to the high Ce^{3+} content, the optimal surface acidity and the unique phase composition.

The very peculiar structure obtained by flame-spray synthesis protects the active species from aging and makes the catalyst resistant to high-temperature treatments. The flame-made catalyst possesses excellent NH_3–SCR performance even after thermal and hydrothermal aging at 700 °C. A deeper investigation of the structural changes upon aging is ongoing.

Finally, this study opens the fundamental issue whether it is possible to produce more active catalytic materials using conventional catalyst preparation methods but with similar structural properties to those obtained here by flame-spray synthesis. Stabilization of a large fraction of Ce^{3+} in rutile TiO_2 and the overall arrangement of the elements that we have described in this work are the key parameter to be optimized.

■ ASSOCIATED CONTENT

Supporting Information

The Supporting Information is available free of charge on the ACS Publications website at DOI: 10.1021/acscatal.5b01580.

Description of the use of $\alpha = NH_3/NO = 1.2$; element mapping by STEM; XPS and XANES fits; NH_3 slip as well NO and NH_3 oxidation experiments (PDF)

■ AUTHOR INFORMATION

Corresponding Authors

*E-mail: k.michalow.mauke@outlook.com.

*E-mail: davide.ferri@psi.ch.

Present Address

¶Solvias AG, Römerpark 2, CH-4303 Kaiseraugst, Switzerland

DOI: 10.1021/acscatal.5b01580
ACS Catal. 2015, 5, 5657–5672

Notes

The authors declare no competing financial interest.

■ ACKNOWLEDGMENTS

The authors would like to thank M. Elsener, A. Marberger, and V. Marchionni for technical support and Dr. F. Krumeich (ETH Zurich) for element mapping. The authors acknowledge support by ScopeM at Swiss Federal Institute of Technology ETHZ, the Electron Microscopy Center of Empa as well as the Swiss Light Source for providing beamtime at the SuperXAS beamline.

■ REFERENCES

(1) Busca, G.; Lietti, L.; Ramis, G.; Berti, F. *Appl. Catal., B* **1998**, *18*, 1−36.
(2) Madia, G.; Elsener, M.; Koebel, M.; Raimondi, F.; Wokaun, A. *Appl. Catal., B* **2002**, *39*, 181−190.
(3) Liu, F.; Yu, Y.; He, H. *Chem. Commun.* **2014**, *50*, 8445−8463.
(4) Zhang, L.; Pierce, J.; Leung, V. L.; Wang, D.; Epling, W. S. *J. Phys. Chem. C* **2013**, *117*, 8282−8289.
(5) Du, X.; Gao, X.; Hu, W.; Yu, J.; Luo, Z.; Cen, K. *J. Phys. Chem. C* **2014**, *118*, 13617−13622.
(6) Chen, J. P.; Yang, R. T. *Appl. Catal., A* **1992**, *80*, 135−148.
(7) Topsøe, N.-Y. *Science* **1994**, *265*, 1217−1219.
(8) Chen, L.; Li, J.; Ge, M. *Environ. Sci. Technol.* **2010**, *44*, 9590−9596.
(9) Chapman, D. M. *Appl. Catal., A* **2011**, *392*, 143−150.
(10) Wachs, I. E.; Kim, T.; Ross, E. I. *Catal. Today* **2006**, *116*, 162−168.
(11) Alemany, L. J.; Lietti, L.; Ferlazzo, N.; Forzatti, P.; Busca, G.; Giamello, E.; Bregani, F. *J. Catal.* **1995**, *155*, 117−130.
(12) Hilbrig, F.; Goebel, H. E.; Knoezinger, H.; Schmelz, H.; Lengeler, B. *J. Phys. Chem.* **1991**, *95*, 6973−6978.
(13) Chen, L.; Weng, D.; Si, Z.; Wu, X. *Prog. Nat. Sci.* **2012**, *22*, 265−272.
(14) Chen, L.; Li, J.; Ge, M.; Zhu, R. *Catal. Today* **2010**, *153*, 77−83.
(15) Xu, W.; Yu, Y.; Zhang, C.; He, H. *Catal. Commun.* **2008**, *9*, 1453−1457.
(16) Gao, X.; Jiang, Y.; Fu, Y.; Zhong, Y.; Luo, Z.; Cen, K. *Catal. Commun.* **2010**, *11*, 465−469.
(17) Li, P.; Xin, Y.; Li, Q.; Wang, Z.; Zhang, Z.; Zheng, L. *Environ. Sci. Technol.* **2012**, *46*, 9600−9605.
(18) Gao, X.; Jiang, Y.; Zhong, Y.; Luo, Z.; Cen, K. *J. Hazard. Mater.* **2010**, *174*, 734−739.
(19) Shan, W.; Liu, F.; He, H.; Shi, X.; Zhang, C. *ChemCatChem* **2011**, *3*, 1286−1289.
(20) Shan, W.; Liu, F.; He, H.; Shi, X.; Zhang, C. *Appl. Catal., B* **2012**, *115*−*116*, 100−106.
(21) Peng, Y.; Li, K.; Li, J. *Appl. Catal., B* **2013**, *140*−*141*, 483−492.
(22) Shan, W.; Liu, F.; He, H.; Shi, X.; Zhang, C. *Chem. Commun.* **2011**, *47*, 8046−8048.
(23) Chaisuk, C.; Wehatoranawee, A.; Preampiyawat, S.; Netiphat, S.; Shotipruk, A.; Mekasuwandumrong, O. *Ceram. Int.* **2011**, *37*, 1459−1463.
(24) Mädler, L.; Kammler, H. K.; Mueller, R.; Pratsinis, S. E. *J. Aerosol Sci.* **2002**, *33*, 369−389.
(25) Teoh, W. Y.; Amal, R.; Mädler, L. *Nanoscale* **2010**, *2*, 1324−1347.
(26) Stark, W. J.; Wegner, K.; Pratsinis, S. E.; Baiker, A. *J. Catal.* **2001**, *197*, 182−191.
(27) Boningari, T.; Koirala, R.; Smirniotis, P. G. *Appl. Catal., B* **2012**, *127*, 255−264.
(28) Boningari, T.; Koirala, R.; Smirniotis, P. G. *Appl. Catal., B* **2013**, *140*−*141*, 289−298.
(29) Jossen, R.; Heine, M. C.; Pratsinis, S. E.; Augustine, S. M.; Akhtar, M. K. *Appl. Catal., B* **2007**, *69*, 181−188.
(30) Michalow-Mauke, K. A.; Lu, Y.; Ferri, D.; Graule, T.; Kowalski, K.; Elsener, M.; Kröcher, O. *Chimia* **2015**, *69*, 220−224.
(31) Akurati, K. K.; Vital, A.; Dellemann, J. P.; Michalow, K.; Graule, T.; Ferri, D.; Baiker, A. *Appl. Catal., B* **2008**, *79*, 53−62.
(32) Michalow, K. A.; Vital, A.; Heel, A.; Graule, T.; Reifler, F. A.; Ritter, A.; Zakrzewska, K.; Rekas, M. *J. Adv. Oxid. Technol.* **2008**, *11*, 56−64.
(33) Devener, B. V.; Anderson, S. L.; Shimizu, T.; Wang, H.; Nabity, J.; Engel, J.; Yu, J.; Wickham, D.; Williams, S. *J. Phys. Chem. C* **2009**, *113*, 20632−20639.
(34) Naumkin, A. V.; Kraut-Vass, S.; Gaarenstroom, W.; Powell, J. C. NIST X-ray Photoelectron Spectroscopy Database at NIST Standard Reference Database 20, Version 4.1. http://srdata.nist.gov/xps/.
(35) Ravel, B.; Newville, M. *J. Synchrotron Radiat.* **2005**, *12*, 537−541.
(36) Koebel, M.; Elsener, M. *Ind. Eng. Chem. Res.* **1998**, *37*, 327−335.
(37) Koebel, M.; Elsener, M. *Chem. Eng. Sci.* **1998**, *53*, 657−669.
(38) Iwaszuk, A.; Nolan, M. *J. Phys. Chem. C* **2011**, *115*, 12995−13007.
(39) Johnston-Peck, A. C.; Senanayake, S. D.; Plata, J. J.; Kundu, S.; Xu, W.; Barrio, L.; Graciani, J.; Sanz, J. F.; Navarro, R. M.; Fierro, J. L. G.; Stach, E. A.; Rodriguez, J. A. *J. Phys. Chem. C* **2013**, *117*, 14463−14471.
(40) Fang, J.; Bi, X.; Si, D.; Jiang, Z.; Huang, W. *Appl. Surf. Sci.* **2007**, *253*, 8952−8961.
(41) Kong, L.; Gregg, D. J.; Karatchevtseva, I.; Zhang, Z.; Blackford, M. G.; Middleburgh, S. C.; Lumpkin, G. R.; Triani, G. *Inorg. Chem.* **2014**, *53*, 6761−6768.
(42) Szymanski, J. T.; Scott, J. D. *Can. Mineral.* **1982**, *20*, 271−280.
(43) Michalow, K. A.; Heel, A.; Vital, A.; Amberg, M.; Fortunato, G.; Kowalski, K.; Graule, T. J.; Rekas, M. *Top. Catal.* **2009**, *52*, 1051−1059.
(44) Hilbring, F.; Schmelz, H.; Knözinger, H. In *Studies in Surface Science and Catalysis*; Guczi, L., Solymosi, F., Tetenyi, P., Eds.; Elsevier: Amsterdam, 1993; Vol. 75, pp 1351−1362.
(45) Jossen, R.; Heine, M. C.; Pratsinis, S. E.; Augustine, S. M.; Akhtar, M. K. *Appl. Catal., B* **2007**, *69*, 181−188.
(46) Shannon, R. D. *Acta Crystallogr., Sect. A: Cryst. Phys., Diffr., Theor. Gen. Crystallogr.* **1976**, *A32*, 751−767.
(47) Shannon, R. D.; Pask, J. R. *J. Am. Ceram. Soc.* **1965**, *48*, 391−398.
(48) Michalow, K. A.; Otal, E. H.; Burnat, D.; Fortunato, G.; Emerich, H.; Ferri, D.; Heel, A.; Graule, T. *Catal. Today* **2013**, *209*, 47−53.
(49) Köger, F. A.; Vink, H. J. *Solid State Phys.* **1956**, *3*, 307−435.
(50) Andersson, D. A.; Simak, S. I.; Skorodumova, N. V.; Abrikosov, I. A.; Johansson, B. *Appl. Phys. Lett.* **2007**, *90*, 031909−1−031909−3.
(51) Albuquerque, A. R.; Bruix, A.; dos Santos, I. M. G.; Sambrano, J. R.; Illas, F. *J. Phys. Chem. C* **2014**, *118*, 9677−9689.
(52) Dutta, G.; Waghmare, U. V.; Baidya, T.; Hegde, M. S.; Priolkar, K. R.; Sarode, P. R. *Chem. Mater.* **2006**, *18*, 3249−3256.
(53) Helean, K. B.; Navrotsky, A.; Lumpkin, G. R.; Colella, M.; Lian, J.; Ewing, R. C.; Ebbinghaus, B.; Catalano, J. G. *J. Nucl. Mater.* **2003**, *320*, 231−244.
(54) Huynh, L. T.; Eger, S. B.; Walker, J. D. S.; Hayes, J. R.; Gaultois, M. W.; Grosvenor, A. P. *Solid State Sci.* **2012**, *14*, 761−767.
(55) Sobaś, P.; Komornicki, S.; Marta, R. *Ceramics, Polish Ceramic Bulletin* **2000**, *61*, 145−154.
(56) Kopia, A.; Kowalski, K.; Chmielowska, M.; Leroux, C. *Surf. Sci.* **2008**, *602*, 1313−1321.
(57) Pfau, A.; Schierbaum, K. D. *Surf. Sci.* **1994**, *321*, 71−80.
(58) Yu, X.; Li, G. *J. Alloys Compd.* **2004**, *364*, 193−198.
(59) Watanabe, S.; Ma, X.; Song, C. *J. Phys. Chem. C* **2009**, *113*, 14249−14257.
(60) Duarte, R. B.; Safonova, O. V.; Krumeich, F.; Makosch, M.; van Bokhoven, J. A. *ACS Catal.* **2013**, *3*, 1956−1964.
(61) Safonova, O. V.; Guda, A. A.; Paun, C.; Smolentsev, N.; Abdala, P. M.; Smolentsev, G.; Nachtegaal, M.; Szlachetko, J.; Soldatov, M. A.; Soldatov, A. V.; van Bokhoven, J. A. *J. Phys. Chem. C* **2014**, *118*, 1974−1982.

DOI: 10.1021/acscatal.5b01580
ACS Catal. 2015, 5, 5657−5672

(62) Bianconi, A.; Marcelli, A.; Dexpert, H.; Karnatak, R.; Kotani, A.; Jo, T.; Petiau, J. *Phys. Rev. B: Condens. Matter Mater. Phys.* **1987**, *35*, 806−812.
(63) Takahashi, Y.; Sakami, H.; Nomura, M. *Anal. Chim. Acta* **2002**, *468*, 345−354.
(64) Busca, G.; Saussey, H.; Saur, O.; Lavalley, J. C.; Lorenzelli, V. *Appl. Catal.* **1985**, *14*, 245−260.
(65) Hadjiivanov, L. *Appl. Surf. Sci.* **1998**, *135*, 331.
(66) Vargas, M. A. L.; Casanova, M.; Trovarelli, A.; Busca, G. *Appl. Catal., B* **2007**, *75*, 303−311.
(67) Bazin, P.; Saur, O.; Lavalley, J. C.; Daturi, M.; Blanchard, G. *Phys. Chem. Chem. Phys.* **2005**, *7*, 187−194.
(68) Millner, T.; Neugebauer, J. *Nature* **1949**, *163*, 601−602.
(69) Jansson, J. In *Urea-SCR technology for deNOx aftertreatment of diesel exhausts*; Nova, I., Tronconi, E., Eds.; Springer: Berlin, 2014; pp 65−96.
(70) Rynkowski, J.; Farbotko, J.; Touroude, R.; Hilaire, L. *Appl. Catal., A* **2000**, *203*, 335−348.
(71) Luo, M.; Chen, J.; Chen, L.; Lu, J.; Feng, Z.; Li, C. *Chem. Mater.* **2001**, *13*, 197−202.

DOI: 10.1021/acscatal.5b01580
ACS Catal. 2015, 5, 5657−5672